

Paleoceanography and Paleoclimatology



RESEARCH ARTICLE

10.1029/2023PA004666

Key Points:

- We use planktic foraminiferal $\delta^{18}\text{O}$ and climate models to infer deglacial changes in the Southern Hemisphere surface westerlies
- We estimate the westerlies were $\sim 5^\circ$ equatorward and $\sim 25\%$ weaker at the LGM; their poleward shift over deglaciation mirrors the rise in CO_2
- Experiments with a $1/4^\circ$ ocean-sea-ice-carbon model indicate increased oceanic carbon storage with equatorward shifted westerlies

Supporting Information:

Supporting Information may be found in the online version of this article.

Correspondence to:

W. R. Gray,
william.gray@lsce.ipsl.fr

Citation:

Gray, W. R., de Lavergne, C., Jnglin Wills, R. C., Menviel, L., Spence, P., Holzer, M., et al. (2023). Poleward shift in the Southern Hemisphere westerly winds synchronous with the deglacial rise in CO_2 . *Paleoceanography and Paleoclimatology*, 38, e2023PA004666. <https://doi.org/10.1029/2023PA004666>

Received 27 APR 2023

Accepted 7 JUN 2023

Author Contributions:

Conceptualization: William R. Gray, Casimir de Lavergne, Robert C. Jnglin Wills, Laurie Menviel, Paul Spence, Elisabeth Michel

Data curation: William R. Gray, Robert C. Jnglin Wills






Funding acquisition: Robert C. Jnglin Wills, Laurie Menviel, Paul Spence, Mark Holzer, Elisabeth Michel

Methodology: William R. Gray, Casimir de Lavergne, Robert C. Jnglin Wills, Laurie Menviel, Paul Spence, Elisabeth Michel

© 2023 The Authors.

This is an open access article under the terms of the [Creative Commons Attribution-NonCommercial License](#), which permits use, distribution and reproduction in any medium, provided the original work is properly cited and is not used for commercial purposes.

Poleward Shift in the Southern Hemisphere Westerly Winds Synchronous With the Deglacial Rise in CO_2

William R. Gray¹ , Casimir de Lavergne², Robert C. Jnglin Wills^{3,4}, Laurie Menviel^{5,6} , Paul Spence^{6,7,8} , Mark Holzer⁹ , Masa Kageyama¹, and Elisabeth Michel¹ 

¹Laboratoire des Sciences du Climat et de l'Environnement (LSCE/IPSL), Université Paris-Saclay, Gif-sur-Yvette, France,

²LOCEAN Laboratory, Sorbonne Université-CNRS-IRD-MNH, Paris, France, ³Institute for Atmospheric and Climate Science, ETH Zurich, Zurich, Switzerland, ⁴Department of Atmospheric Sciences, University of Washington, Seattle, WA, USA, ⁵Climate Change Research Centre, University of New South Wales, Sydney, NSW, Australia, ⁶The Australian Centre for Excellence in Antarctic Science, University of Tasmania, Hobart, TAS, Australia, ⁷Institute for Marine and Antarctic Studies, University of Tasmania, Hobart, TAS, Australia, ⁸Australian Antarctic Partnership Program, University of Tasmania, Hobart, TAS, Australia, ⁹School of Mathematics and Statistics, University of New South Wales, Sydney, NSW, Australia

Abstract The Southern Hemisphere westerly winds influence deep ocean circulation and carbon storage. While the westerlies are hypothesized to play a key role in regulating atmospheric CO_2 over glacial-interglacial cycles, past changes in their position and strength remain poorly constrained. Here, we use a compilation of planktic foraminiferal $\delta^{18}\text{O}$ from across the Southern Ocean and emergent relationships within an ensemble of climate models to reconstruct changes in the Southern Hemisphere surface westerlies over the last deglaciation. We infer a 4.8° ($2.9\text{--}7.1^\circ$, 95% confidence interval) equatorward shift and about a 25% weakening of the westerlies during the Last Glacial Maximum (20 ka) relative to the mid-Holocene (6.5 ka). Climate models from the Palaeoclimate Modeling Intercomparison Project substantially underestimate this inferred equatorward wind shift. According to our reconstruction, the poleward shift in the westerlies over deglaciation closely mirrors the rise in atmospheric CO_2 ($R^2 = 0.98$). Experiments with a 0.25° resolution ocean-sea-ice-carbon model suggest that shifting the westerlies equatorward reduces the overturning rate of the ocean below 2 km depth, leading to a suppression of CO_2 outgassing from the polar Southern Ocean. Our results support a role for the westerly winds in driving the deglacial CO_2 rise, and suggest outgassing of natural CO_2 from the Southern Ocean is likely to increase as the westerlies shift poleward due to anthropogenic warming.

Plain Language Summary The mid-latitudes of the Southern Hemisphere are characterized by a band of strong westerly winds. These winds play an important role in driving the circulation of the deep ocean and are thought to influence the oceans' ability to store carbon. Understanding how the westerlies have varied in the past is challenging as we have few methods to track the winds directly. Here we use oxygen isotopes in foraminiferal shells to track changes in the broad-scale pattern of sea surface temperature across the Southern Ocean, which we link to changes in the winds using climate models. We find the westerly winds were displaced around 5° equatorward during the cold climate of the last ice age, and that the poleward shift in the winds we observe as the earth warmed out of the ice age bears an uncanny resemblance to the increase in atmospheric CO_2 . We then force the winds in a climate model toward the equator in a similar manner to the shift we observe in the ice age, and find the model stores more carbon in the ocean. Our results support a link between shifts in the Southern Hemisphere westerly winds and atmospheric CO_2 .

1. Introduction

The Southern Hemisphere westerly winds play a key role in returning deep ocean waters to the surface and thus largely govern the rate at which the deep oceanic reservoirs of heat and carbon communicate with the surface ocean and atmosphere (Marshall & Speer, 2012; Toggweiler & Samuels, 1995). South of $\sim 47^\circ\text{S}$ the modern westerly winds drive divergent Ekman transports that contribute to lift deepwaters and tilt density surfaces (Toggweiler & Samuels, 1995). Although mesoscale ocean eddies work to flatten the steep isopycnals, the counteraction of the wind-driven circulation by the eddies is incomplete, resulting in a residual circulation that brings macro-nutrient and carbon rich deepwaters to the surface (Abernathy et al., 2011; Marshall & Speer, 2012). Due to iron (Martin et al., 1990) and light (Mitchell et al., 1991) limitation the upwelled nutrients are not completely utilized before buoyancy loss near the Antarctic continent causes some of the upwelled waters to sink as Antarctic Bottom

Validation: Mark Holzer, Masa Kageyama
Visualization: William R. Gray, Casimir de Lavergne, Laurie Menviel
Writing – original draft: William R. Gray, Casimir de Lavergne
Writing – review & editing: William R. Gray, Casimir de Lavergne, Robert C. Jnglin Wills, Laurie Menviel, Paul Spence, Mark Holzer, Masa Kageyama, Elisabeth Michel

Water, filling the deep ocean with “preformed” nutrients (Ito & Follows, 2005; Pasquier & Holzer, 2016). This “leak” in the biological pump, largely caused by the over-supply of nutrients to the surface ocean by wind-driven upwelling, leads to the hypothesis that changes in the Southern Hemisphere westerly winds could help regulate atmospheric CO₂ over glacial-interglacial cycles (Ai et al., 2020; Anderson et al., 2009; Lauderdale et al., 2017; Sigman & Boyle, 2000; Toggweiler et al., 2006).

Past changes in the position and strength of the Southern Hemisphere westerly winds are poorly constrained, making it difficult to assess their role in driving past carbon cycle changes. A compilation of diverse proxy data suggests signals of an equatorward shift in the westerlies during the Last Glacial Maximum (LGM, 19–23 ka) relative to the Holocene (Kohfeld et al., 2013). However, relating changes in the measured proxies (i.e., terrestrial moisture, marine productivity) to the position of the westerlies is challenging, both quantitatively and qualitatively, such that even the direction of change during the LGM (i.e., poleward vs. equatorward) is debated (Sime et al., 2013, 2016). Furthermore, while climate models show a relatively clear and consistent signal of an equatorward shift in the Northern Hemisphere surface westerlies under glacial forcings (Gray et al., 2020; Kageyama et al., 2020; Li & Battisti, 2008) in agreement with proxy data (Gray et al., 2020), they show little consistency in the magnitude or sign of change in the Southern Hemisphere (Chavaillaz et al., 2013; Kageyama et al., 2020; Sime et al., 2013). Ice core data suggest abrupt shifts in the westerlies during the millennial scale atmospheric CO₂ variability of the last glacial period (Buizert et al., 2018), but there is currently little constraint on how or when the westerlies shifted over the last deglaciation (20–10 ka), as atmospheric CO₂ rose by ~90 ppmv (Marcott et al., 2014).

To reconstruct changes in the position of the Southern Hemisphere westerly winds over the last deglaciation we exploit the two-way basin-scale coupling between the westerly winds and the meridional gradients in sea surface temperature (SST) at mid-latitudes (Nakamura et al., 2004; Yang et al., 2020). At the latitude where the meridional SST gradient is steepest, baroclinicity in the lower atmosphere is elevated, initiating baroclinic storm track eddies that converge zonal momentum and anchor the surface westerlies (Nakamura et al., 2008). The westerly wind stress in turn drives ocean current systems that maintain the steep SST gradient, closing the feedback loop (Nakamura et al., 2004, 2008). This two-way coupling implies that the latitude of maximum zonal-mean zonal wind stress (hereafter referred to as *wind latitude*) should be related to the latitude of maximum meridional gradient of zonal-mean SST (hereafter referred to as *SST front latitude*) across broad sectors of the Southern Ocean (Nakamura et al., 2008; Yang et al., 2020).

To track changes in the Southern Ocean SST front latitude over the deglaciation we use a basin-wide compilation of $\delta^{18}\text{O}$ in planktic foraminiferal calcite ($\delta^{18}\text{O}_{\text{calcite}}$; Figure 1). Although $\delta^{18}\text{O}_{\text{calcite}}$ is a function of both temperature and the $\delta^{18}\text{O}$ of seawater ($\delta^{18}\text{O}_{\text{water}}$), the effect of temperature is around six times greater than the effect of $\delta^{18}\text{O}_{\text{water}}$ at the basin scale (Figure S1 in Supporting Information S1). As no physical mechanism exists to drive such large changes in $\delta^{18}\text{O}_{\text{water}}$ at the basin scale, and as the Southern Ocean meridional pattern of $\delta^{18}\text{O}_{\text{water}}$ is itself closely linked to the SST pattern via the influence of downgradient moisture fluxes on net precipitation (Siler et al., 2018), the meridional pattern of $\delta^{18}\text{O}_{\text{calcite}}$ will always be dominated by temperature and tightly coupled to the meridional SST profile (Figure S1 in Supporting Information S1). Meridional profiles of $\delta^{18}\text{O}_{\text{calcite}}$ thus allow us to identify and track the SST front latitude (Gray et al., 2020) (Figure 1). We use an ensemble of climate models to establish an “emergent” relationship (i.e., an empirical, multi-model, relationship) (Eyring et al., 2019; Hall et al., 2019) between the SST front latitude and the wind latitude. We first test the skill of this model-derived relationship, before combining it with the reconstructed changes in the SST front latitude to quantify shifts in the surface westerlies over deglaciation. Finally, we perform new experiments with a ¼ degree ocean-sea ice-carbon cycle model to better understand the impact of wind shift on the residual circulation and biogeochemistry of the Southern Ocean.

2. Methods

2.1. New and Compiled Planktic Foraminiferal $\delta^{18}\text{O}$ Data From the Southern Ocean

We compiled existing records of planktic foraminiferal $\delta^{18}\text{O}$ from near-surface dwelling species from core sites across the Southern Ocean, and generated new data from cores in the Kerguelen plateau and southeast Pacific (Figures 1a and 1b; Figures S2 and S3 in Supporting Information S1). We generated new planktic foraminiferal $\delta^{18}\text{O}$ records from two sediment cores retrieved from the Kerguelen Plateau during cruise OSCAR INDIEN-SUD

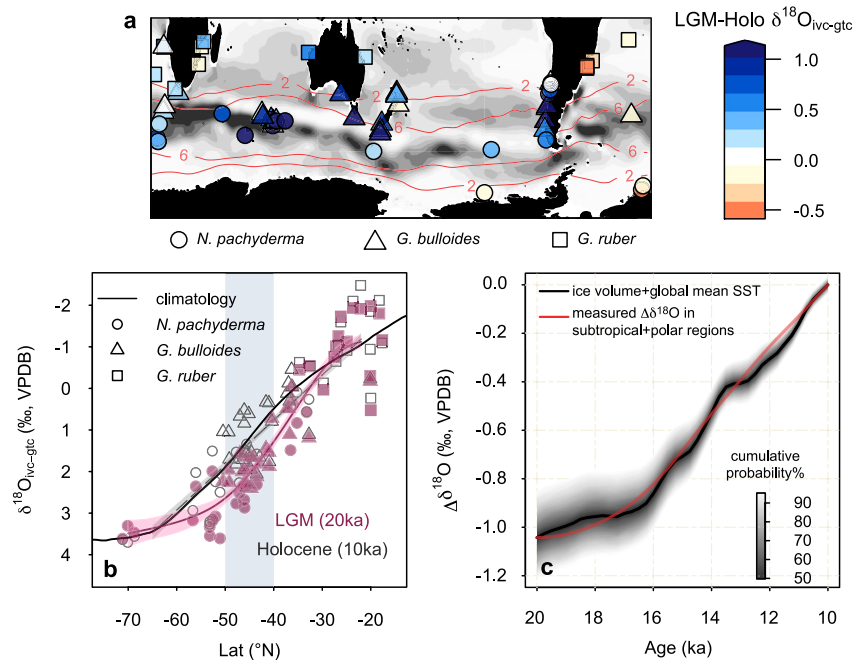


Figure 1. $\delta^{18}\text{O}$ data and whole ocean changes. (a) LGM-Holocene $\delta^{18}\text{O}_{\text{ivc-gtc}}$ ($\delta^{18}\text{O}_{\text{calcite}}$ corrected for ice volume and global-mean SST changes; Section 2) at the core sites. The modern climatological meridional $\delta^{18}\text{O}$ gradient is represented by the background shading (Figure S1 in Supporting Information S1; darkest shade represents 0.25‰/°Lat , equivalent to $\sim 1\text{°C/°Lat}$). The red contours show modern annual-mean near-surface zonal wind speed in m/s (Figure S1 in Supporting Information S1). (b) Meridional profiles Holocene (dashed/gray) and Last Glacial Maximum (solid/pink) $\delta^{18}\text{O}_{\text{ivc-gtc}}$. The data are fit with a generalized additive model. Error envelopes show $\pm 1\text{SE}$. The modern climatological zonal-mean $\delta^{18}\text{O}_{\text{calcite}}$ profile is shown by the solid black line (Figure S1 in Supporting Information S1). The gray box shows the latitudinal window in which $\Delta\text{Lat}_{\text{SST}}$ is calculated. Symbols on (a) and (b) distinguish foraminiferal species. (c) Whole ocean $\delta^{18}\text{O}$ corrections calculated from the change in $\delta^{18}\text{O}$ from global ice volume and global mean SST change ($\delta^{18}\text{O}_{\text{ivc-gtc}}$), and the measured change in $\delta^{18}\text{O}_{\text{calcite}}$ in the combined polar ($>65\text{°S}$) and subtropical ($<25\text{°S}$) portions of the meridional $\delta^{18}\text{O}$ profiles (Figures S2 and S3 in Supporting Information S1), uncorrected for whole-ocean effects on $\delta^{18}\text{O}$. The impact of shifts in the westerlies is substantially smaller in these regions compared to the mid-latitudes, such that they should broadly reflect the whole ocean changes rather than local dynamics.

(MD12-3396CQ, -47.73°N , 87.69°E ; MD12-3401CQ, -44.68°S , 80.39°E). Furthermore, we extended/increased the resolution of two previously published records from cores located on Kerguelen (MD02-2488, -51.07°N , 67.73°E) and in the southeast Pacific (MD07-3119, -46.08°N , -76.1°E). We analyzed $\delta^{18}\text{O}$ on either *Globigerina bulloides* or *Neogloboquadrina pachyderma* using a GV Isoprime 100 and an OPTIMA, and a Finnigan MAT251 and a $\Delta+$ at the Laboratoire des Sciences du Climat et de l'Environnement (LSCE). The measurements are reported versus Vienna Pee Dee Belemnite (VPDB) standard defined with respect to the NBS19 standard. The mean external reproducibility (1σ) of carbonate standards is $\pm 0.06\text{‰}$ for $\delta^{18}\text{O}$; the different mass spectrometers are regularly inter-calibrated and the data are corrected, depending on the devices, for nonlinearity and the common acid bath. Within this internal calibration, NBS18 is $-23.2\text{‰} \pm 0.2\text{‰}$ VPDB for $\delta^{18}\text{O}$ and $-5.0\text{‰} \pm 0.1\text{‰}$ VPDB for $\delta^{13}\text{C}$. Age models for all the cores are based on radiocarbon dating, and further details of the age models can be found in Haddam et al. (2020) for core MD07-3119 and Gottschalk et al. (2020) for core MD12-3396CQ. Reservoir age changes for the Kerguelen area followed results to establish the age model of core MD12-3401CQ (Gottschalk et al., 2020). The new data are provided in Table S1 and are available on Pangaea (<https://doi.org/10.1594/PANGAEA.932846>).

We compiled all available existing $\delta^{18}\text{O}$ records for near-surface dwelling planktic foraminifera species (*Globigerinoides ruber*, *G. bulloides*, *N. pachyderma*; Supporting Information S1) spanning the last deglaciation (10–20 ka) from across the Southern Ocean (Bostock et al., 2004, 2015; Caley et al., 2011; Calvo et al., 2007; Caniupán et al., 2011; Carlson et al., 2008; Charles et al., 1991; Chiessi et al., 2014; Crosta et al., 2004; Dyez et al., 2014; Fischer & Wefer, 1999; Gersonde et al., 2003; Gottschalk et al., 2015, 2018; Govin et al., 2009; Grobe & Mackensen, 1992; Haddam et al., 2018; Hasenfratz et al., 2019; Hodell et al., 2000, 2003; Labeyrie et al., 1996;

Lamy et al., 2004; Levi et al., 2007; Lu et al., 2016; Martínez-Méndez et al., 2010; Mashiotta et al., 1999; Mohtadi et al., 2008; Nelson et al., 2000; Pereira et al., 2018; Pichon et al., 1992; Portilho-Ramos et al., 2018; Rickaby & Elderfield, 1999; Santos et al., 2017; Sarin et al., 1994; Schiraldi et al., 2014; Schneider et al., 1995; Scussolini & Peeters, 2013; Sicre et al., 2005; Sikes et al., 2009; Stuut et al., 2002, 2019; Y. V. Wang et al., 2013; Winn, 2013; Zahn et al., 1994). The compiled records are kept on the original age model of publication. Together, the new and compiled data amount to 64 deglacial records of planktic foraminiferal $\delta^{18}\text{O}$. All $\delta^{18}\text{O}$ data are given in Table S1 and are available on Pangaea (<https://doi.org/10.1594/PANGAEA.932846>).

2.2. Tracking the SST Front Latitude

Meridional shifts in the SST front ($\Delta\text{Lat}_{\text{SST}}$) are calculated by finding the latitudinal shift that minimizes the difference between the $\delta^{18}\text{O}$ profile at each time step and the Holocene $\delta^{18}\text{O}$ profile, within a 10° latitudinal window that includes the steepest part of the profile (Gray et al., 2020) (Figure 1b and Figures S2 and S3 in Supporting Information S1). We account for whole ocean changes in $\delta^{18}\text{O}_{\text{water}}$ and the global-mean SST change ($\delta^{18}\text{O}_{\text{ivc-gtc}}$; Figure 1c), quantifying uncertainties via bootstrapping and Monte-Carlo simulation. We compute $\Delta\text{Lat}_{\text{SST}}$ across the entire Southern Ocean, as well as separately in the Indian-Pacific and Atlantic sectors (Figure 2), and regional subsets (Section 3.3); given the paucity of data from south of 65°S we include Antarctic marginal sites from all sectors in all regional subsets. The R code and data used to perform the analysis is provided at <https://doi.org/10.5281/zenodo.7866501>. The $\Delta\text{Lat}_{\text{SST}}$ reconstructions are provided in Tables S2 and S3.

In detail, the analyses were performed as follows: we first interpolate the $\delta^{18}\text{O}$ data to a 250-year time grid extending from 20 to 10 ka using a Generalized Additive Model (GAM) (Wood, 2011), with the smoothing term determined by restricted maximum likelihood (Wood et al., 2016). The reader is referred to Simpson (2018) for an overview of GAMs. Only foraminiferal $\delta^{18}\text{O}$ records that span the entire time period of the reconstruction are utilized such that our analysis compares relative changes in the same records through time; as such both the spatial distribution and the species composition of the $\delta^{18}\text{O}$ data remain constant at all timesteps. The mean temporal resolution of the individual records over deglaciation is about 1 point per 250 years, and we only include $\delta^{18}\text{O}_{\text{calcite}}$ records with a minimum of 1 point per 1 ka over the deglaciation.

We model the $\delta^{18}\text{O}$ data at each time step (first correcting for whole-ocean effects, see below) as a function of latitude using a GAM in the same manner as described above (Figures S2 and S3 in Supporting Information S1). We compute the shift in latitude which minimizes the Euclidean distance (L^2) between the GAM fit at each time step relative to 10 ka, within a 10° latitude band centered around the steepest part of the Holocene meridional SST/ $\delta^{18}\text{O}_{\text{calcite}}$ profile ($40\text{--}50^\circ\text{S}$; gray box in Figure 1b; Figures S2 and S3 in Supporting Information S1). The width of this latitudinal band has a negligible impact on our results. The 10 ka reference time is chosen to maximize the number of records spanning the deglaciation. Note, we use this method to track the position of the SST front latitude through time, rather than directly locating the latitude of maximum gradient in $\delta^{18}\text{O}_{\text{calcite}}$ in the same way we locate the SST front in model output (see Section 3.2), because this method was demonstrated to perform better with proxy data (Gray et al., 2020).

To minimize temporal changes in the meridional $\delta^{18}\text{O}_{\text{calcite}}$ profile that arise from whole-ocean changes rather than regional dynamics we correct the $\delta^{18}\text{O}_{\text{calcite}}$ data for the whole-ocean change in $\delta^{18}\text{O}_{\text{water}}$ (arising from ice sheet growth/retreat) and the global-mean SST change ($\delta^{18}\text{O}_{\text{ivc-gtc}}$) (Figure 1c). For the whole-ocean change in $\delta^{18}\text{O}_{\text{water}}$ we scale the LGM-Holocene change of $1.0 \pm 0.1\text{‰}$ (2σ) (Schrag et al., 2002) by the sea level curve of Lambeck et al. (2014). For the global-mean SST change we scale the $-1.7 \pm 1.0^\circ\text{C}$ (2σ) area-weighted global-mean LGM-preindustrial change in SST from the Paleoclimate Modeling Intercomparison Project (PMIP) 3 and 4 ensemble (see Section 2.3; note, the recent multi-model data assimilation of Annan et al. (2022) falls within this range), by the global temperature record of Shakun et al. (2012), using the water-calcite temperature fractionation ($\delta^{18}\text{O}_{\text{calcite-water}}$) of Kim and O'Neil (1997), which agrees with the pooled-foraminiferal species sensitivity of Malevich et al. (2019). We propagate the uncertainty from these whole-ocean corrections through to our final results. We note these whole-ocean corrections make the reconstructed changes in the position of the SST front more conservative; removing the global-mean SST change correction entirely results in an Indian-Pacific $\Delta\text{Lat}_{\text{SST}}$ of $\sim 7^\circ$ between 10 and 20 ka (cf. $\sim 5^\circ$ including the correction). The $\delta^{18}\text{O}_{\text{calcite}}$ evolution in the subtropical and polar sectors (i.e., the regions where we expect the dynamically driven changes to be substantially smaller relative to the mid-latitudes; Figures S2 and S3 in Supporting Information S1) shows excellent agreement in both magnitude and timing with the whole-ocean $\delta^{18}\text{O}$ corrections we are applying (Figure 1c), confirming these whole-ocean corrections are unlikely to be introducing substantial artifacts into the reconstruction. Our

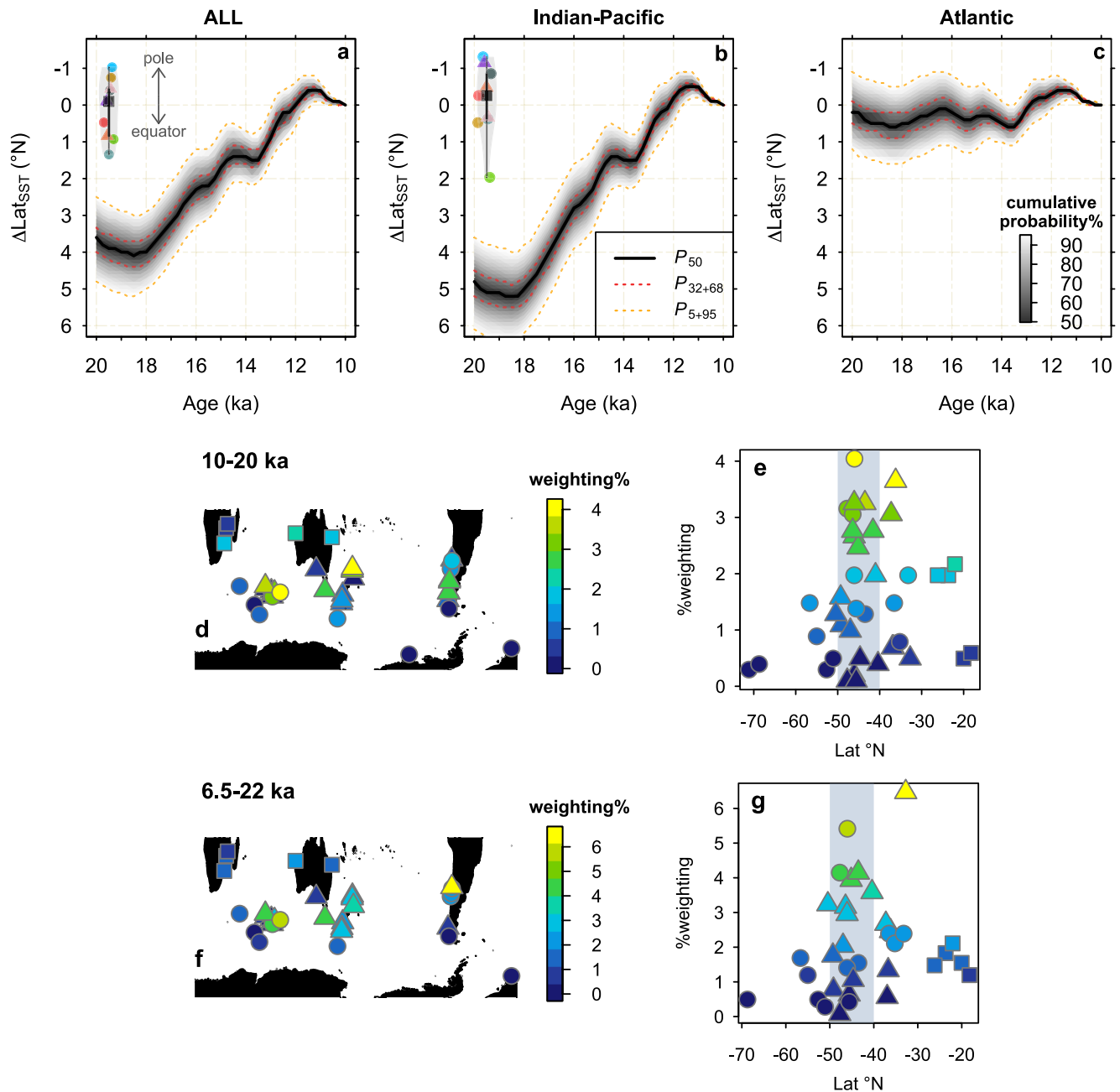


Figure 2. $\Delta\text{Lat}_{\text{SST}}$ within different sectors and core weightings in the Indian-Pacific sector. Change in the SST front latitude ($\Delta\text{Lat}_{\text{SST}}$) from 20 to 10 ka using (a) all data from across the Southern Ocean, and in the (b) Indian-Pacific and (c) Atlantic sectors separately. The 5th, 32nd, 50th, 68th, and 95th percentiles are indicated. The colored symbols on (a) and (b) show the residual change in LGM-PI SST front latitude in each model within the ensemble. The residual change is calculated as the change in SST front latitude beyond the expected change in SST front latitude given the change in wind latitude within the same model (Section 3.2; Figure 5), and the relationship between the two parameters (Figures 3a and 3b). Colors represent individual models; see Figures 3, 5, or 8 for key to individual models. The ensemble mean is shown by the black square. The shaded area shows the distribution of the uncertainty about the mean, with the black lines showing the 68% and 95% CI. Our reconstructed shift in SST front latitude is significantly larger than the residual change in SST front latitude during the Last Glacial Maximum seen in any of the individual models. Contribution of each record to the Indian-Pacific $\Delta\text{Lat}_{\text{SST}}$ reconstruction based on leave-one-out analysis. (d–e) 10–20 ka reconstruction (f–g) 6.5–22 ka reconstruction. Note Antarctic marginal sites from the Atlantic sector are also included given the paucity of data from south of 65°S. Symbols distinguish species of planktic foraminifera (circles = *N. pachyderma*, triangles = *G. bulloides*, squares = *G. ruber*).

leave-one-out analysis (Section 3.1) shows that our reconstruction is primarily driven by mid-latitude sites, further indicating these whole-ocean corrections are unlikely to be biasing our results. Finally, the lack of change in the $\Delta\text{Lat}_{\text{SST}}$ reconstruction in the Atlantic (Figure 2) also demonstrates that these whole-ocean corrections do not induce apparent shifts in the position of the SST front.

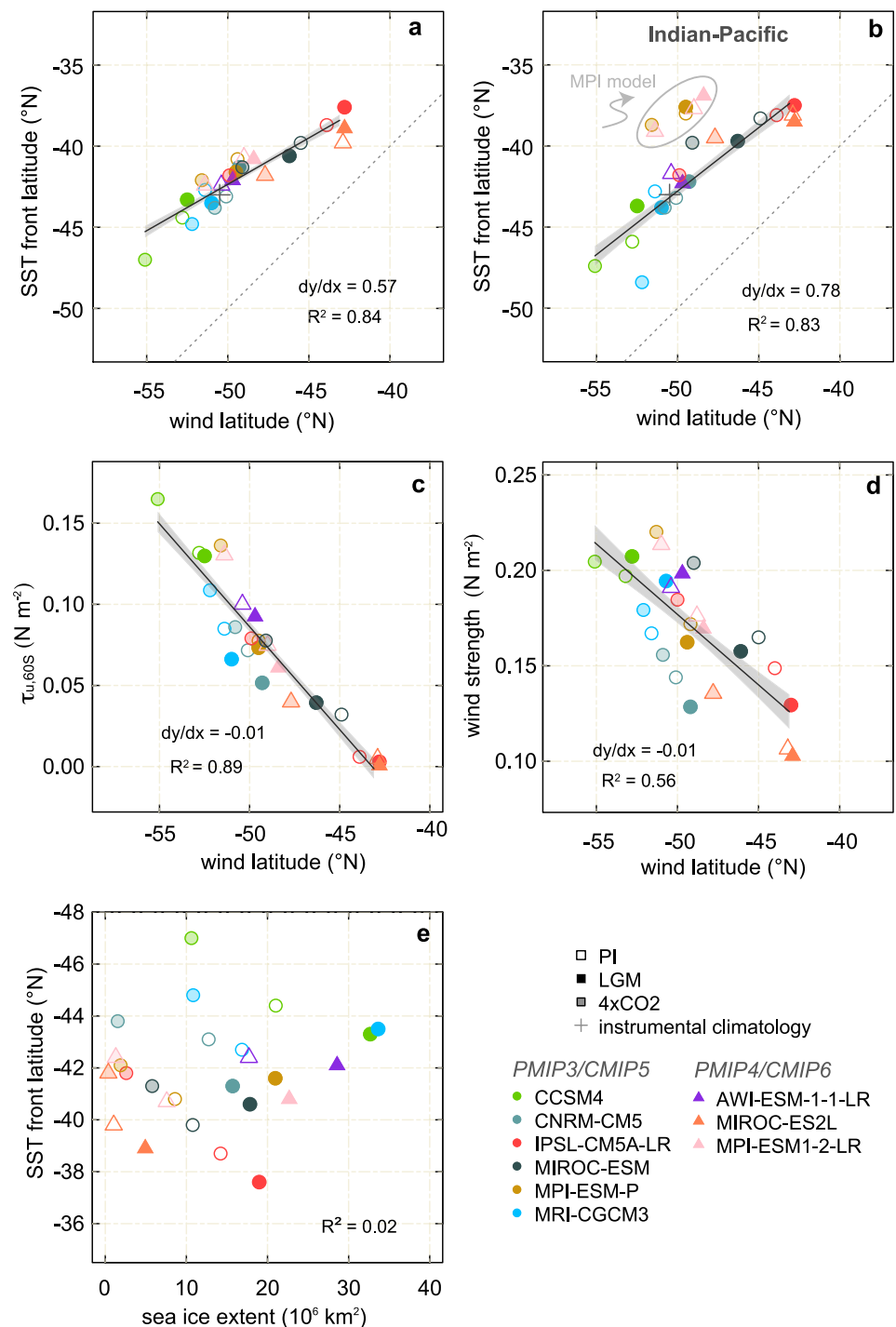


Figure 3. Emergent relationships in the PMIP3/4 and CMIP5/6 ensemble. (a) Relationship between the wind latitude (latitude of maximum zonal-mean zonal wind stress) and SST front latitude (latitude of maximum meridional gradient in zonal-mean SST, within a 10° latitudinal window) within the PMIP3/CMIP5 and PMIP4/CMIP6 ensemble. Error envelope shows $\pm 1SE$. Note the 5° offset between the axes. (b) Relationship between the zonal-mean wind latitude and SST front latitude across the Indian and Pacific sectors. The MPI model sits as an outlier from the rest of the ensemble, and is excluded from the regression. Including the MPI model has a negligible impact on our results. (c) Relationship between wind latitude and zonal-mean wind stress at 60° S ($\tau_{u,60S}$). (d) Relationship between wind latitude and wind strength (maximum zonal-mean τ_u). (e) Relationship between SST front latitude and sea ice extent (area with $>15\%$ annual mean sea ice concentration).

We derive uncertainties via bootstrap resampling of the data set (Efron, 1979) (10,000 iterations), also accounting for the age and analytical uncertainties on individual records as well as the uncertainties in the whole-ocean change in $\delta^{18}\text{O}_{\text{water}}$ and the global-mean SST change with Monte-Carlo simulation. We ascribe age uncertainties of $\pm 1,000$ years (2σ), and analytical uncertainties of $\pm 0.08\text{‰}$ (2σ) to all planktic foraminiferal $\delta^{18}\text{O}$ records. When calculating the lead-lag between our $\Delta\text{Lat}_{\text{SST}}$ reconstruction and the change in atmospheric CO_2 and the global temperature over deglaciation (Section 3.4) we account for age uncertainties in the CO_2 record using the typical gas age uncertainty in the West Antarctic Ice Sheet Divide ice core over deglaciation (± 75 years, 1σ ; Sigl et al., 2016). For the age uncertainty in the global mean temperature stack we take the uncertainty in the lag of global temperature over CO_2 (± 340 years, 1σ) from Shakun et al. (2012). To account for age uncertainties in the $\Delta\text{Lat}_{\text{SST}}$ reconstruction, we repeat the lead-lag analysis using each bootstrap/Monte-Carlo iteration of the $\Delta\text{Lat}_{\text{SST}}$ reconstruction. This approach assumes age uncertainties within the $\delta^{18}\text{O}$ compilation are uncorrelated, which is unlikely given for example, reservoir age changes in the Southern Ocean (although methodological differences between studies add a source of random “human behavioral” error), but still provides a first-order assessment of leads and lags between the different time series.

To assess shifts in the westerlies within the early Holocene we repeat the analysis over a longer time period (6.5–22 ka) which necessitates using a smaller subset of cores and thus results in larger uncertainties (Figure S4 in Supporting Information S1). Still, the results show excellent agreement with the complete set of cores (i.e., spanning 10–20 ka) (Figure S4 in Supporting Information S1), with a slope of 0.95 during the overlapping interval. We correct for this difference in slope in the longer reconstruction, though the correction makes a negligible difference and does not impact our conclusions (Figure S4 in Supporting Information S1). Performing the analysis further into the Holocene (2.5–22 ka) results in substantially higher uncertainties due to the small number of cores spanning this interval, but the results suggest the SST front latitude/westerlies are relatively stable through the late Holocene (Figure S4 in Supporting Information S1), in agreement with qualitative indicators of the winds (Buizert et al., 2018; Lamy et al., 2010; Saunders et al., 2018).

2.3. PMIP3/4 and CMIP5/6 Climate Model Ensemble

We use an ensemble of climate models from PMIP3 (Braconnot et al., 2012) and PMIP4 (Kageyama et al., 2018, 2020) and Coupled Model Intercomparison Project (CMIP) 5 (Taylor et al., 2012) and 6 (Eyring et al., 2016); data available at <https://esgf-node.llnl.gov/projects/esgf-llnl/>. We use all CMIP5/PMIP3 and CMIP6/PMIP4 models for which both SST and zonal surface wind fields are available for the LGM and preindustrial (PI) simulations, and also include the $4 \times \text{CO}_2$ simulations from these models where available. Annual-mean climatologies are calculated from the final 100 years of each simulation (years 51–150 of the $4 \times \text{CO}_2$ simulation) and interpolated to a common 2° analysis grid.

We calculate the SST front latitude as the latitude of maximum meridional gradient in zonal-mean SST in each simulation within a 10° latitudinal averaging window. The zonal mean SST is first smoothed using a 10° running mean (to eliminate small-scale variability). The SST front is then defined where the smoothed SST profile has the largest meridional gradient. This definition focuses on the broad-scale mid-latitude meridional temperature gradient, similar to previous work (Yang et al., 2020), and is thus broader than, and distinct from, oceanic fronts associated with the Antarctic Circumpolar Current (ACC) (Chapman et al., 2020). We use zonal-mean SST across the Southern Ocean (Figure 3a) and across regional subsets (Figures 3b and 4; Figure S5 in Supporting Information S1). We calculate the wind latitude as the latitude of maximum zonal-mean zonal wind stress, the wind strength as the maximum in zonal-mean zonal wind stress, and the sea ice extent as the area with $>15\%$ annual-mean sea ice concentration.

The model ensemble allows us to quantify emergent relationships (empirical, multi-model, relationships) (Eyring et al., 2019; Hall et al., 2019) between wind latitude and SST front latitude (Figures 3a, 3b, and 4), wind latitude and wind strength (Figure 3c), and wind latitude and zonal-mean zonal wind stress at 60°S ($\tau_{u,60\text{S}}$; Figure 3d). We will test the skill of the emergent relationship between wind latitude and SST front latitude (Section 3.3; Figure 4), before combining it with reconstructed changes in the SST front latitude ($\Delta\text{Lat}_{\text{SST}}$) to quantify past shifts in the wind latitude ($\Delta\text{Lat}_{\text{wind}}$). We then estimate changes in wind strength and $\tau_{u,60\text{S}}$ using the reconstruction of wind latitude and the emergent relationships with these properties.

2.4. Wind-Shift Experiments With a 0.25° Ocean-Sea-Ice-Carbon Model

We use the ocean-sea-ice-carbon model MOM5-SIS-Wombat with a Mercator horizontal resolution of 0.25° (~ 11 km grid spacing at 65°S), and 50 vertical levels (Hogg et al., 2017; Menviel et al., 2018). The model

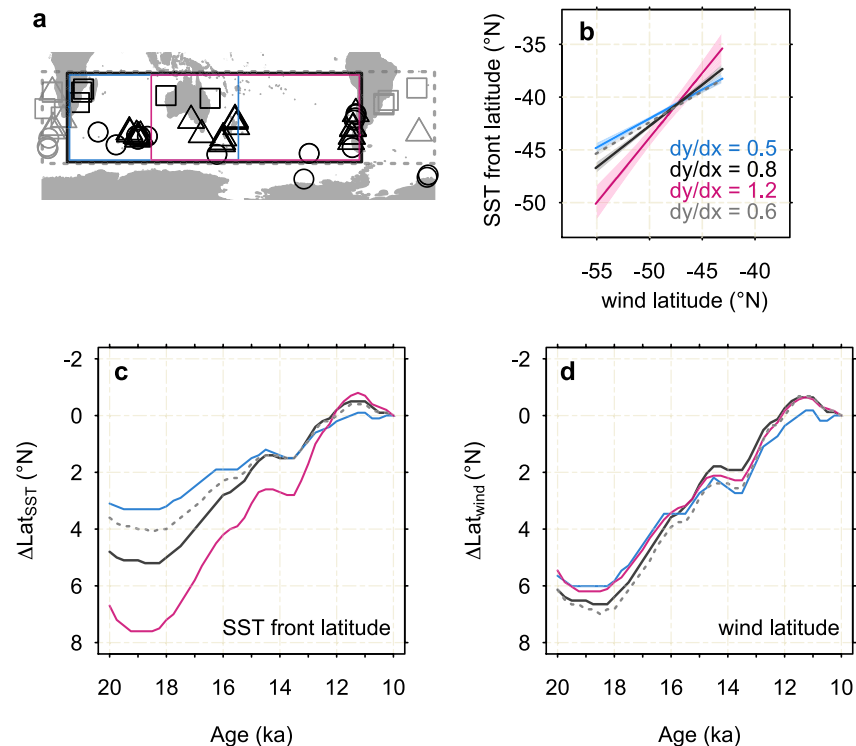


Figure 4. SST front and westerly wind changes based on regional subsets (a) Map showing regional subsets. Light gray dashed line corresponds to all core sites. Black includes all Indian-Pacific sites, blue has eastern Pacific sites removed, while pink has western Indian sites removed. Note that given the paucity of data from south of 65°S we include Antarctic marginal sites from all sectors in all regional subsets. (b) Relationship between zonal-mean wind latitude and regional SST front latitude within the model ensemble. Shading shows $\pm 1SE$. (c) Reconstructed change in SST front latitude (ΔLat_{SST}) within the regional subsets. (d) Reconstructed zonal-mean wind latitude (ΔLat_{wind}) calculated from the regional ΔLat_{SST} reconstruction (c) and the relationships between regional SST front latitude and zonal-mean wind latitude given in (b).

is initialized with modern-day temperature and salinity distributions, and biophysical fields derived from an observation-based climatology (GLODAP v2; Olsen et al., 2016). The model is then spun-up for 700 years with version 2 of the Coordinated Ocean-ice Reference Experiments Normal Year Forcing reanalysis data (Griffies et al., 2009), representative of a “normal year” during the recent instrumental period. To study the impact of equatorward shifted southern westerlies, a 4° equatorward shift (with no change in magnitude) is applied to the near-surface wind speeds between 25°S and 70°S. The perturbation simulation is run for 125 years. Anomalies are calculated as the difference between the average of the last 10 years of the Perturbed experiment and the concomitantly extended Control experiment to remove the influence of model drift. Both experiments are forced with the same atmospheric temperatures and precipitation, so that SST and buoyancy fluxes do not freely adjust to the shifted winds in the Perturbed experiment. Our experimental design thus precludes a comprehensive assessment of feedback effects between ocean dynamics and buoyancy balance that play an important role in setting the equilibrium state of the real ocean (Abernathy et al., 2011; Bishop et al., 2016).

The model includes parameterizations for the effects of mesoscale eddies on tracer and mass transports. The isopycnal tracer diffusivity (Redi, 1982) is constant at $600 \text{ m}^2 \text{ s}^{-1}$. The isopycnal thickness diffusivity (Gent & McWilliams, 1990) is independent of depth but varies horizontally and temporally with the simulated stratification (it is proportional to the product of local Rossby radius squared and Eady growth rate). These diffusivities are imperfect surrogates for the effects of mesoscale eddies, and may therefore introduce bias in the simulated circulation and its sensitivity. However, the dependence of the isopycnal thickness diffusivity on local quantities relevant to baroclinic instability enables appropriate sensitivity of the simulated overturning to wind changes (Gent, 2016). Additionally, realistic eddy-rich models indicate that the bulk of southward flow across the ACC is accomplished by mean geostrophic flows rather than transient eddies (Dufour et al., 2015; Mazloff et al., 2013), and that the Southern Ocean residual overturning responds sensitively to polar Ekman flows (Bishop et al., 2016; Dufour et al., 2012; Stewart et al., 2021). Consistent with these expectations, we find that resolved advection

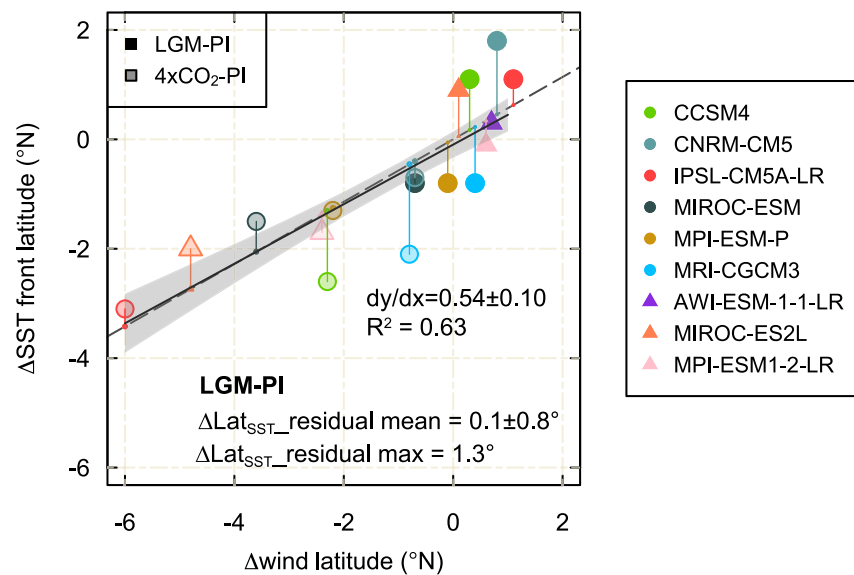


Figure 5. LGM-PI and $4 \times \text{CO}_2$ -PI changes in SST front latitude and wind latitude in the model ensemble. The dashed gray line shows the relationship between SST front latitude and wind latitude across the ensemble incorporating the absolute differences in climatology between the models (equivalent to the regression line in Figure 3a). The solid black line shows the regression line between the $\Delta(\text{wind latitude})$ and $\Delta(\text{SST latitude})$ across the ensemble; this is statistically indistinguishable from the relationship incorporating the absolute differences in climatology between the models (Figure 3a), suggesting the coupling between the winds and SST front is a particularly robust feature of the climate model ensemble. Finally, the residuals of the LGM-PI changes (indicated with colored vertical lines) are randomly distributed, indicating the ensemble shows no bias away from the expected relationship between SST front latitude and wind latitude under Last Glacial Maximum forcing.

dominates both the deep southward flow across the ACC and the response to wind shift (Figures S6 and S7 in Supporting Information S1). Parameterized advection (representing the impact of eddies on mass transports) plays only a minor role in the overturning change (Figure S7 in Supporting Information S1). We also find a small change in the ACC strength: the eastward transport through Drake Passage is 122 Sv in the last decade of the Perturbed experiment, compared to 130 Sv in the same decade of the Control experiment (a 6% decrease).

3. Results and Discussion

3.1. Reconstructed Changes in the SST Front Latitude

Our analysis of the data reveals an equatorward shift in the SST front during the LGM (20 ka) relative to 10 ka (Figures 1b and 2; Figures S2 and S3 in Supporting Information S1), indicative of an equatorward shift in the winds. Mapping the LGM $\delta^{18}\text{O}_{\text{ivc-glc}}$ anomalies shows a large mid-latitude cooling during the LGM across the Indian and Pacific sectors (Figure 1a; equivalent to a cooling of $4\text{--}5^\circ\text{C}$ beyond the global-mean SST change indicated by the model ensemble). Our Indian-Pacific $\Delta\text{Lat}_{\text{SST}}$ reconstruction shows a 4.8° ($3.6\text{--}6.1^\circ$ 95% confidence interval [CI]) equatorward shift in the SST front during the LGM relative to 10 ka (Figure 2b). We perform a jack-knife (leave-one-out) resampling of the data set to determine the contribution of each planktic foraminiferal $\delta^{18}\text{O}$ record to the Indian-Pacific $\Delta\text{Lat}_{\text{SST}}$ reconstruction. We sequentially remove each record from the data set, recompute $\Delta\text{Lat}_{\text{SST}}$, and determine the contribution of that record as the time-integrated absolute difference from $\Delta\text{Lat}_{\text{SST}}$ computed using the entire data set (expressed as a percentage of the absolute cumulative change in $\Delta\text{Lat}_{\text{SST}}$ over deglaciation). This analysis shows that no single record contributes more than 5% of the total variance, and that the cores with the highest weighting are all located in the mid-latitudes (Figures 2d–2g), indicating the Indian-Pacific $\Delta\text{Lat}_{\text{SST}}$ reconstruction primarily reflects a mid-latitude signal.

By contrast, we find a slight warming anomaly (relative to the global-mean LGM SST change) at all latitudes in the western Atlantic (Figure 1a), possibly a signal of a weakened Atlantic Meridional Overturning Circulation (AMOC) (Gherardi et al., 2009; Stocker & Johnsen, 2003), and no significant change in the SST front latitude within the Atlantic sector over deglaciation (Figure 2c). This result is consistent with a weak relationship between the SST front latitude and wind latitude in the eastern Atlantic, where the vast majority of the Atlantic

mid-latitude cores are located (Figure 1a; Figure S5 in Supporting Information S1). This weak relationship might owe to bathymetric constraints on the latitude of the confluence of warm Indian Ocean waters and colder Southern Ocean waters south of Africa. Although we attribute the lack of change in the SST front latitude within the Atlantic to the partial decoupling of the westerlies and SST front there, we cannot rule out that the westerlies did not shift substantially over deglaciation within the Atlantic. Given the lack of sensitivity of SST front latitude in the Atlantic (Figure S5 in Supporting Information S1), we use the Indian-Pacific $\Delta\text{Lat}_{\text{SST}}$ timeseries (Figure 2b) to reconstruct shifts in the zonal-mean wind latitude over deglaciation. We note that also including the Atlantic data (Figure 2a) makes no substantial difference to the reconstruction of zonal-mean wind latitude (Section 3.3), but slightly increases the error.

3.2. Emergent SST Front-Wind Latitude Relationship and Coupling Dynamics

Pre-industrial, LGM, and $4 \times \text{CO}_2$ simulations from the ensemble of models from the PMIP3/PMIP4 and CMIP5/CMIP6 model ensemble demonstrate a tight zonal-mean relationship between wind latitude and SST front latitude over a wide range of climate states (Figure 3a; $R^2 = 0.84$). The wind latitude is located 3–10° poleward of the SST gradient latitude (Figure 3a), a consequence of the poleward drift of storm track eddies during their lifecycle (Tamarin & Kaspi, 2016). The relationship between the wind latitude and the SST front latitude has a slope of less than one, presumably because it is modulated by the influence of bathymetry and oceanic eddies on upper-ocean currents and SST (Dong et al., 2006; Kohfeld et al., 2013). These processes can cause local decoupling between the winds and SST gradient (Figure 1a), yet the coupling holds on a hemispheric scale (Nakamura et al., 2004, 2008) (Figures 3a and 3b).

The coupling mechanism between the winds and SST front is primarily due to the atmospheric response to ocean SST gradient anomalies, which is why it is also found in atmosphere-only models (Nakamura et al., 2008). However, the response of the surface ocean circulation acts as a feedback (via its influence on the SST gradient) and the coarse-resolution models employed here use parameterizations (Gent & McWilliams, 1990; Redi, 1982) for the effects of oceanic mesoscale eddies, which could lead to bias (i.e., structural uncertainty) in the emergent relationship. Coarse-resolution ocean models tend to overestimate the response of the ACC to wind changes (Bishop et al., 2016; Downes & Hogg, 2013). Should this bias lead to an overestimated slope in the relationships shown in Figures 3a and 3b, then our reconstruction of the SST front latitude would imply an even larger change in the wind latitude over deglaciation. Nevertheless, several factors support the robustness of the emergent relationship (Figures 3a and 3b): (a) the presently defined SST front is distinct from the ACC and is expected to be more tightly coupled to wind shifts than the volume transport of the circumpolar current or the position of its major fronts (cf. Figure S5c in Supporting Information S1; Figure 3a); (b) the relationship does not stem only from model responses, but also from contrasting climatologies of the models under identical forcing (compare IPSL-CM5A-LR and CCSM4 under PI forcings in Figure 3a); (c) the regional subset test (Section 3.3 below) shows consistency between our proxy-based regional reconstructions of the SST front latitude and regional relationships within the model ensemble (Figure 4).

To assess whether some aspect of the LGM climate (i.e., global cooling, expanded Antarctic sea ice; Sime et al., 2016) may cause a deviation away from the emergent relationship between wind latitude and SST front latitude (Figures 3a and 3b), we calculate the LGM-PI changes in SST front latitude and wind latitude within each individual model in the ensemble (Figure 5). This approach effectively normalizes for the inter-model differences in preindustrial climatology which drive much of the variance in the relationship (Figure 3a). We then calculate the residual change in SST front latitude during the LGM as the difference from the change expected using the relationship shown in Figure 3a. We find a mean residual of $0.1 \pm 0.8^\circ$ across the ensemble (i.e., within error of zero), implying that the ensemble moves along the relationship of Figure 3a between PI and LGM states. This indicates that there is no a priori reason to expect deviation away from the emergent relationship under glacial boundary conditions (e.g., due to an expansion of Antarctic sea ice). The largest residual change in SST front latitude within any of the individual models under glacial forcings is 1.3° ; this is significantly smaller than the reconstructed LGM shift in SST front latitude, such that an equatorward shift in the westerlies is robust to even the largest of the individual LGM-PI residuals (Figures 2a and 2b). Finally, we find no correlation between Antarctic sea ice extent and the SST front latitude in the model ensemble (Figure 2e; $R^2 = 0.02$), nor do we find a correlation between sea ice extent and the wind latitude ($R^2 = 0.03$).

3.3. Quantifying Wind Shift From the SST Front Latitude

We apply the emergent relationship between wind latitude and SST front latitude in the Indian-Pacific sector (Figure 2b) to our Indian-Pacific $\Delta\text{Lat}_{\text{SST}}$ reconstruction to quantify shifts in the zonal-mean wind latitude over

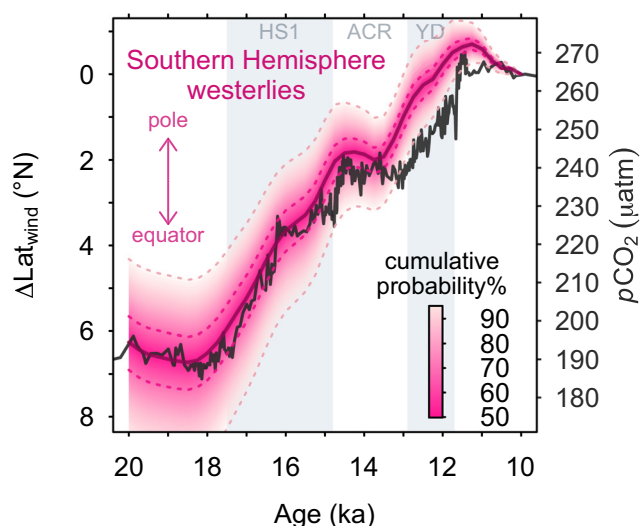


Figure 6. Deglacial shifts in the zonal-mean surface westerlies and atmospheric CO_2 . Deglacial change in the position of the wind latitude ($\Delta\text{Lat}_{\text{wind}}$, pink lines show the 5th, 32nd, 50th, 68th, and 95th percentiles) and atmospheric CO_2 (Marcott et al., 2014) over time before present. HS1, ACR, and YD are Heinrich Stadial 1, Antarctic Cold Reversal, and Younger-Dryas, respectively.

the deglaciation ($\Delta\text{Lat}_{\text{wind}}$). We propagate the uncertainty in the relationship between SST front and wind latitude through to our final estimates of $\Delta\text{Lat}_{\text{wind}}$ using a Monte-Carlo approach (Section 2.2). The area-minimizing method used to track the SST front in the $\delta^{18}\text{O}_{\text{calcite}}$ data (Gray et al., 2020) cannot be directly applied to the model ensemble because the SST climatologies differ across models. However, it is possible to apply this minimization method to LGM-PI and $4 \times \text{CO}_2$ -PI differences within each model. We thus calculated $\Delta\text{Lat}_{\text{SST}}$ for each of these model differences using both methods (area-minimization and maximum gradient of zonal-mean SST); this comparison shows good agreement between the two methods, with a residual standard error of $<0.5^\circ$ and a slope within uncertainty of one (0.99 ± 0.08). Hence, the difference in the two methods used to locate the SST front is unlikely to bias our results. To account for the difference in the way the SST front latitude is determined in data and models we propagate this “methodological uncertainty” through to our final reconstruction of $\Delta\text{Lat}_{\text{wind}}$. The $\Delta\text{Lat}_{\text{wind}}$ reconstruction is provided in Tables S2 and S3.

To ascertain whether the model ensemble has skill in predicting the relationship between regional SST front latitude and zonal-mean wind latitude, we first attempt reconstructions of $\Delta\text{Lat}_{\text{wind}}$ using regional subsets (Figure 4a); we sequentially remove regional subsets of cores from the compilation (Figure 4a), re-compute $\Delta\text{Lat}_{\text{SST}}$ (Figure 4c), and recalculate the relationship between the zonal-mean wind latitude and the regional SST front latitude (Figure 4b). We find that although different regions yield differing magnitudes of deglacial change in SST front latitude (Figure 4c), they yield almost

identical changes in zonal-mean wind latitude (Figure 4d), given the region-specific relationship between the two (Figure 4b). This convergence of the $\Delta\text{Lat}_{\text{wind}}$ reconstructions (Figure 4d) suggests that the emergent relationship is not biased by the models' imperfect representation of the effects of bathymetry and eddies on the meridional SST gradient, such that any structural uncertainty is likely to be small. If biases in these processes were important, the large variations in bathymetry and eddies across sectors of the Southern Ocean (Thompson & Naveira Garabato, 2014) would be expected to lead to disagreements between the regional $\Delta\text{Lat}_{\text{wind}}$ reconstructions. Combining the measured shifts in SST front latitude with the emergent relationship between wind latitude and SST front latitude therefore provides a robust constraint on the zonal-mean wind latitude.

Finally, we excluded the MPI model from the regressions for the Indian-Pacific sector (Figure 2b), as this model sits as an outlier from the remainder of the ensemble (however the slope between wind latitude SST front latitude within the MPI model is consistent with the rest of the ensemble), possibly relating to meridional heat transport biases in the Indian sector (Fathrio et al., 2017), where we find the largest difference relative to the other models. Including the MPI model in the Indian-Pacific sector regression has a negligible effect on our results, slightly increasing the reconstructed change in wind latitude ($\Delta\text{Lat}_{\text{wind}}$) between 10 and 20 ka from 6.2° to 6.7° and increasing the uncertainty by 0.5° at the 95% CI. Removing the MRI model, which contains a previously identified issue with wind stress over sea-ice (Marzocchi & Jansen, 2017), makes no difference to our results.

3.4. Deglacial Shifts in the Surface Westerlies

We infer a 6.3° (4.3 – 8.7° , 95% CI) equatorward shift in the wind latitude during the LGM (20 ka) relative to 10 ka (Figure 6). The evolution of the wind latitude over deglaciation closely mirrors, and is highly correlated with ($R^2 = 0.98$), the evolution of atmospheric CO_2 (Marcott et al., 2014; Figure 6). We calculate the lead-lag between the Indian-Pacific $\Delta\text{Lat}_{\text{SST}}$ reconstruction and the change in atmospheric CO_2 and global temperature over deglaciation as the time offset that maximizes the correlation between the two time series, broadly following the approach of Shakun et al. (2012). This suggests a 330 ± 230 years (95% CI) lead in changes in the winds over changes in CO_2 , and a $1,460 \pm 670$ years lead in the winds over global temperature change. As a sensitivity test, we repeat the lead-lag analysis including varying degrees of “structural” age uncertainty in the Indian-Pacific $\Delta\text{Lat}_{\text{SST}}$ reconstruction to account for the likely correlation of radiocarbon reservoir age uncertainties within the compilation. This suggests that the lead in the change in the winds over CO_2 is significant at the 95% level until

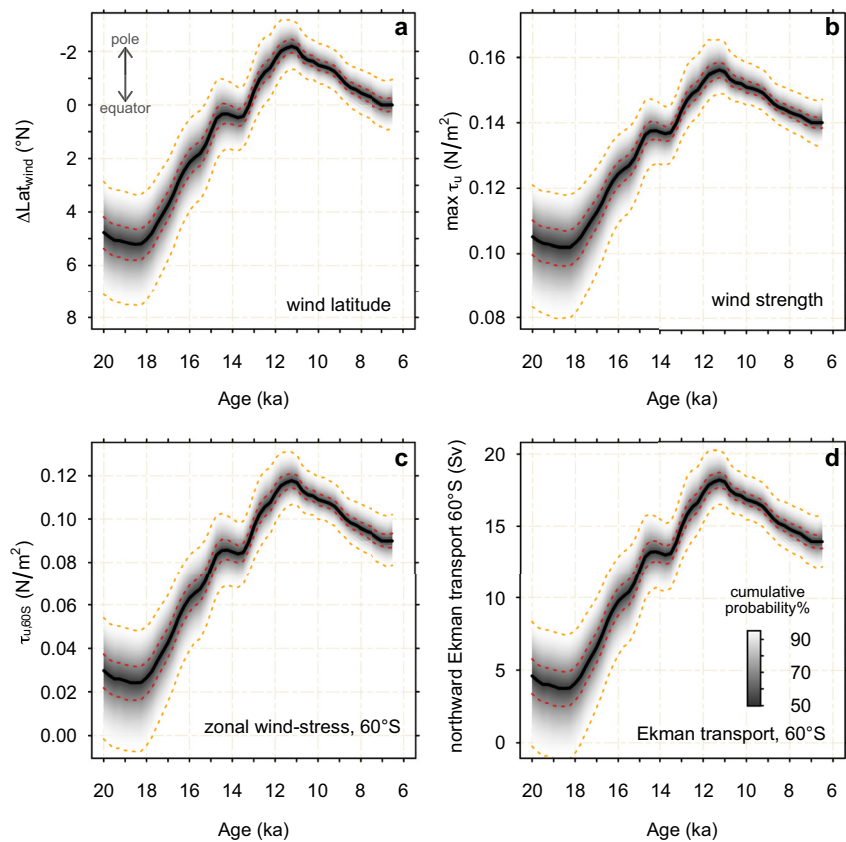


Figure 7. Changes in wind latitude, wind strength, wind stress at 60°S and northward Ekman transport at 60°S from the Last Glacial Maximum to mid-Holocene. Reconstructed changes in (a) wind latitude ($\Delta\text{Lat}_{\text{wind}}$) (b) wind strength ($\max \tau_u$) (c) zonal-mean zonal wind stress at 60°S ($\tau_{u,60S}$) (d) northward Ekman transport at 60°S. Note, these reconstructions cover a longer time period than Figure 6. (b) and (c) are calculated using the reconstructed changes in wind latitude (a) and the relationships between wind latitude and these parameters in the model ensemble (Figure 3). Northward Ekman transport at 60°S is calculated using zonal wind stress at 60°S. The 5th, 32nd, 50th, 68th, and 95th percentiles are indicated. The displayed uncertainties account for uncertainty in the emergent relationships between pairs of variables due to variations across the model ensemble.

more than ~30% of the age uncertainty is correlated across the compilation (assuming 100% of the age uncertainty is correlated, i.e., perfect covariance, results in uncertainties of ± 860 years [95% CI]). The reconstruction indicates a greater lead of $\Delta\text{Lat}_{\text{SST}}$ relative to CO_2 after the Antarctic Cold Reversal (~14 ka; Figure 3). To test whether the lead of $\Delta\text{Lat}_{\text{SST}}$ relative to CO_2 holds in the early deglaciation, we repeat this analysis for 20–14 ka (cf. 20–10 ka) and find a lead of 160 years (–10–330 years, 95% CI), compared to 330 years (100–560 years, 95% CI) over the entirety of the deglaciation. The planktic foraminiferal $\delta^{18}\text{O}$ compilation used in this study will benefit from any future improvements in our knowledge of regional radiocarbon reservoir ages (and their spatial covariance), which may lead to adjustments in the precise phasing between the inferred wind shifts and atmospheric CO_2 .

Our analysis over a longer time interval indicates an early Holocene extremum in the poleward position of the wind latitude, followed by a $\sim 1.5^\circ$ equatorward shift in the winds over 10–6.5 ka (Figure 7a). Despite the larger uncertainties in the early Holocene reconstruction, it agrees well with the analysis of the full data set (i.e., 10–20 ka) in the overlapping sections (Figure S4 in Supporting Information S1). Our results thus indicate a 4.8° (2.9 – 7.1° , 95% CI) equatorward shift of the surface westerlies during the LGM (20 ka) relative to the mid Holocene (6.5 ka) (Figure 7a). Overall, while our results confirm the tendency of climate models to shift the winds poleward in a warming climate (Yin, 2005), the magnitude of the inferred LGM to mid-Holocene wind shift is substantially greater than that predicted by any of the models within the PMIP3/4 ensemble between LGM and preindustrial states (Figure 8).

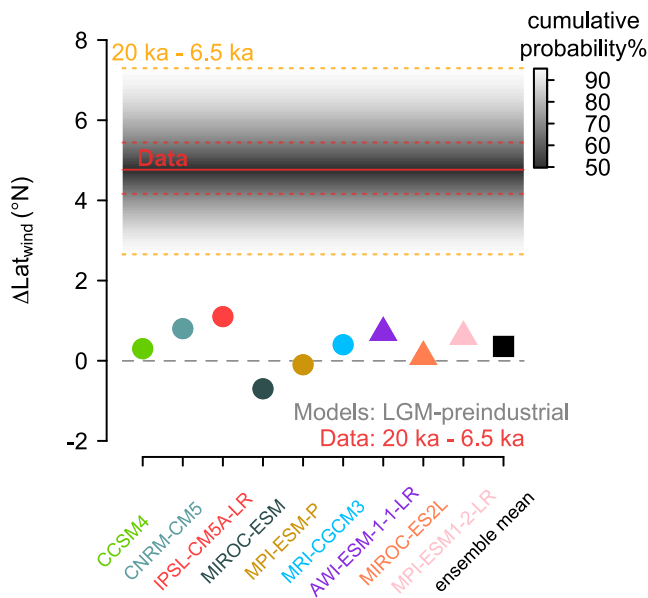


Figure 8. LGM-PI change in the PMIP3/4 ensemble. LGM-PI change in wind latitude in the PIMP3 (circles) and PMIP4 (triangles) simulations, compared to the reconstructed change in $\Delta\text{Lat}_{\text{wind}}$ for the period 20–6.5 ka.

3.5. Reconstructing Wind Strength

The climate model ensemble shows a correlation between the wind latitude and the maximum magnitude of the zonal-mean zonal wind stress (*wind strength*; Figure 3d). The tendency for the peak westerly wind stress to decrease as the winds move equatorward (and vice-versa) has been previously noted (Barnes & Polvani, 2013). Using our $\Delta\text{Lat}_{\text{wind}}$ reconstruction and the emergent relationship between wind latitude and wind strength, we estimate changes in the wind strength over deglaciation (Figure 7b), propagating the uncertainties in the $\Delta\text{Lat}_{\text{wind}}$ reconstruction and in the relationship between the two variables via Monte-Carlo simulation. Our reconstructed equatorward shift in the wind latitude implies a weakening of the peak westerly wind stress by 0.034 N m^{-2} (about 25%) during the LGM relative to the mid Holocene, resulting in a LGM wind strength of 0.106 ($0.085\text{--}0.12$, 95% CI) N m^{-2} , assuming mid-Holocene wind strength is equal to the modern climatology (0.14 N m^{-2}). This assumption is supported by qualitative tracers of the westerlies (Buizert et al., 2018; Lamy et al., 2010; Saunders et al., 2018) which indicate little change between ~6.5 ka and the present day, and by running our analysis further into the Holocene which shows little change in the position of the winds, although uncertainties are large (Figure S4 in Supporting Information S1). We note that as the mechanism underlying the relationship between wind position and wind strength remains partly unclear (Barnes & Polvani, 2013; McGraw & Barnes, 2016), the reconstructed changes in wind strength are more tentative than the reconstructed changes in wind latitude. The wind strength ($\max \tau_w$) reconstruction is provided in Table S3.

The model ensemble shows little change in the shape of meridional wind profile between PI and LGM states; there is a $-0.25\% \pm 7\%$ and $0.5\% \pm 3.5\%$ ensemble mean change in peak width at 50% and 15% peak height, respectively, between LGM and PI. Furthermore, we observe no significant relationship between the wind latitude and the peak width (at either 50% or 15% peak height) within the ensemble, such that we do not expect substantial changes in the shape of the zonal mean wind profile as the winds shift.

3.6. Modeled Impacts of Wind Shift on Ocean Circulation and Biogeochemistry

The similarity of the changes in reconstructed wind latitude and atmospheric CO_2 over the deglaciation (Figure 6) reinforces the hypothesis of their coupling through Southern Ocean circulation and carbon cycling (Toggweiler et al., 2006). While modeling studies typically show a consistent increase in oceanic carbon storage following a weakening of the westerlies, the impact of shifts in the latitude of the westerlies is more ambiguous (Gottschalk et al., 2019; Lauderdale et al., 2017). However, only global models with a resolution of 1° or coarser have been used to study the impact of equatorward wind shift to date (Gottschalk et al., 2019; Lauderdale et al., 2017), possibly limiting the sensitivity of the simulated Southern Ocean overturning circulation (Hallberg & Gnanadesikan, 2006; Spence et al., 2009). To better understand how changes in the latitude of the westerlies may affect the oceanic overturning circulation and carbon cycle, we performed two experiments with a global ocean-sea-ice-carbon model with 0.25° horizontal resolution: a Control experiment is forced by climatological atmospheric forcing representative of the recent instrumental period; a Perturbed experiment uses the same forcing except for a uniform 4° equatorward shift of the Southern Hemisphere westerlies, with no change in their magnitude. Because the wind stress forcing in the perturbation experiment does not include the 25% reduction in wind strength (and is smaller than our reconstructed LGM shift) this simulation represents a conservative assessment of the impacts of an equatorward wind shift alone. The 125-year transient response does not allow quantification of the equilibrium response of the deep ocean nutrient and carbon cycles (Lauderdale et al., 2017). Nevertheless, it reveals clear trends in circulation and biogeochemistry which provide an indication of how the rapidly responding Ekman transports may reorganize the overturning and qualitatively impact the carbon cycle on longer timescales.

We find a complete suppression of CO_2 outgassing south of 60°S in the Perturbed experiment (Figures 9 and 10), with only a partial compensation further north. As such, there is an anomalous uptake of 27 GtC by the Southern Ocean south of 35°S over the course of the Perturbed experiment, equivalent to an atmospheric CO_2 decrease of 13 ppm (Figures 9 and 10). Deepwater upwelling and surface nutrient and carbon concentrations are substantially

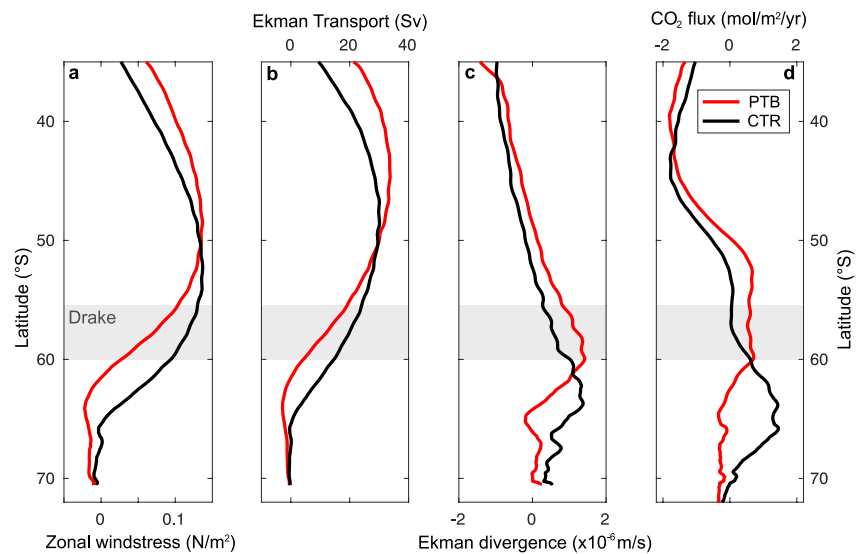


Figure 9. Modeled impact of equatorward shifted westerlies on Southern Ocean CO₂ outgassing. Zonally averaged (a) zonal wind stress, (b) northward Ekman transport, (c) Ekman divergence and, (d) ocean-atmosphere CO₂ flux (positive for ocean outgassing). Black curves correspond to the Control state (CTR) and red curves to the average over years 116–125 of the Perturbed experiment (PTB). Gray shading on (a–d) indicates the latitudes of the Drake Passage (56–60°S). 1 Sv = 10⁶ m³ s⁻¹.

reduced south of 60°S (Figures 9 and 10), indicating that reduced exposure of nutrient and carbon rich deepwaters in the polar Southern Ocean underpins the simulated carbon cycle response to equatorward-shifted westerlies (Supporting Information S1).

With the winds shifted equatorward relative to their modern position, northward Ekman transports become more divergent north of about 60°S, but less divergent south of 60°S (Figure 9). In our simulation, this results in a substantial decrease in upwelling within the polar Southern Ocean (Figure 9) and a slowdown of the global residual circulation deeper than 2 km (Figure 11; Figure S6 in Supporting Information S1). The decrease in deep-ocean overturning results in increased storage of carbon and regenerated nutrients below ~1.5 km depth, concurrent with a decrease in dissolved oxygen (Figures 11 and 12). Conversely, we see an increase in upwelling north of 60°S and increased overturning in the upper ocean, concurrent with decreased carbon concentrations in the upper ~1.5 km.

Hence, although shifting the winds equatorward increases the overall Ekman divergence across the Southern Ocean (Figures 9c and 11a), it focuses the wind's energy away from isopycnals outcropping carbon-rich

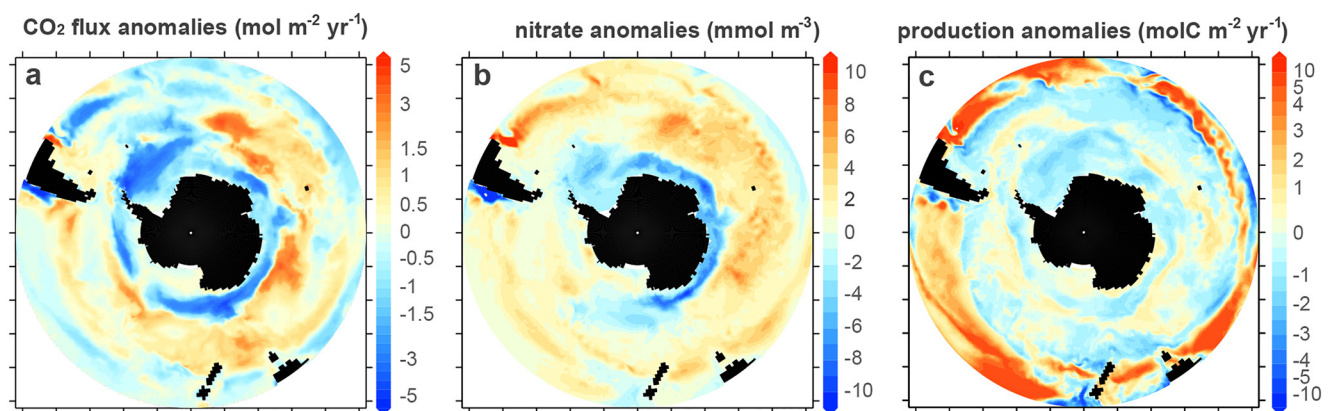


Figure 10. Modeled impact of equatorward shifted westerlies on Southern Ocean surface biogeochemistry. Perturbed-Control difference anomalies of (a) ocean-atmosphere CO₂ flux (mol m⁻² yr⁻¹, positive flux for ocean outgassing) and (b) surface nitrate (mmol m⁻³, averaged over upper 149 m depth) (c) vertically integrated (over the upper 149 m) gross phytoplankton production (molC m⁻² yr⁻¹). Shown quantities are averaged over years 116–125 of each experiment.

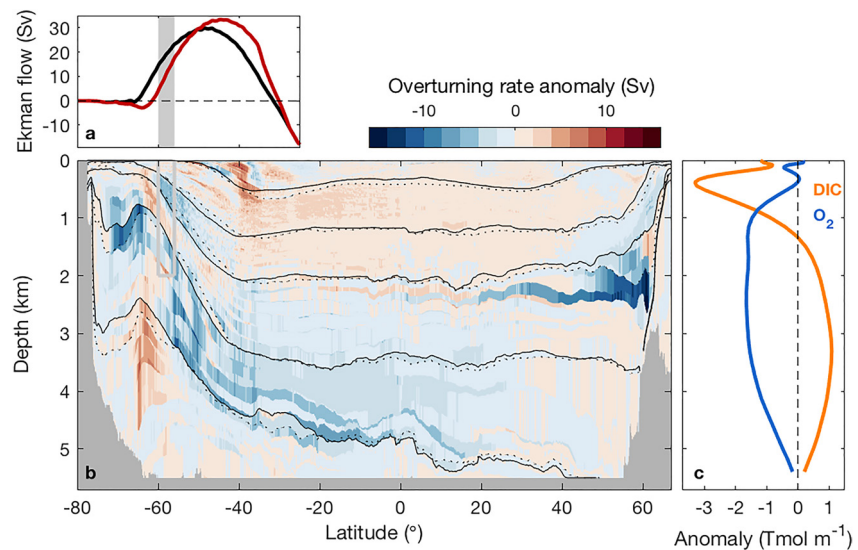


Figure 11. Modeled impact of equatorward shifted westerlies on deep ocean circulation and carbon storage. (a) Northward Ekman transport in the Control (black) and Perturbed (red) simulations. $1 \text{ Sv} = 10^6 \text{ m}^3 \text{ s}^{-1}$. (b) Anomaly (Perturbed-Control) of the absolute value of global meridional overturning streamfunction after 125 years. We quantify changes in absolute values such that blue is a decrease and red is an increase in the magnitude of the overturning rate. Contours show Control (solid) and Perturbed (dashed) isopycnals. (c) Dissolved Inorganic Carbon and Oxygen (O_2) anomalies (Perturbed-Control global horizontal integrals). Zonally averaged concentration anomalies are shown in Figure 12. Gray shading on (a) and (b) indicates the Drake Passage. The meridional overturning circulation shown above (and in Figure S6 in Supporting Information S1) includes both resolved and parameterized advection (Figure S7 in Supporting Information S1). It is calculated in neutral density (Jackett & McDougall, 1997) coordinate and reprojected onto the depth coordinate (Zika et al., 2013) in order to eliminate adiabatic recirculations and avoid spurious effects due to vertical inversions in potential density fields.

deepwaters, toward lighter isopycnals containing relatively less carbon, leading to a net increase in oceanic carbon storage (Figure 11c). In contrast, some previous studies using coarse-resolution models simulated a decrease in oceanic carbon storage in response to an equatorward shift in the westerlies (Gottschalk et al., 2019; Lauderdale et al., 2017). We attribute this difference to the response of the residual overturning in the Southern Ocean, which is likely better captured in our 0.25° simulation (Hallberg & Gnanadesikan, 2006; Spence et al., 2009), but acknowledge that other factors (particularly the short length of our simulations) may contribute to the discrepancy.

3.7. Preformed Nutrients, Nutrient Deepening, and Long-Term CO_2 Drawdown

The reduction in upwelling within the polar Southern Ocean causes the preformed nitrate concentration of Antarctic Bottom Water to decrease (Figure 12). This may be enhanced by a shoaling of the polar Southern Ocean mixed layer depth within the simulation (Figure S8 in Supporting Information S1; Figure 10), providing a potential mechanism to further increase the utilization of the upwelled nutrients via reduced light limitation (Mitchell et al., 1991). Driven by mixed layer shoaling in deepwater formation regions of the North Atlantic (Figure S8 in Supporting Information S1), the preformed nitrate concentration of the northern end member also decreases. As such, the ocean's preformed nutrient inventory begins to decrease, while the regenerated nutrient content increases, leading to a 1.3% increase in global mean N^* ($N^* = \text{regenerated } \text{NO}_3 / \text{total } \text{NO}_3$) after 125 years (Figure 12b). Assuming these transient changes are indicative of the long-term trend, they imply a long-term increase in the efficiency of the biological pump and decrease in atmospheric CO_2 (Ito & Follows, 2005; Lauderdale et al., 2017).

While the short duration of the Perturbed experiment inhibits a full quantification of the CO_2 response, extrapolating the initial changes in endmember preformed NO_3 based on the relative volume of the ocean each endmember represents we can broadly estimate the magnitude of CO_2 change implicated by the initial changes in endmember preformed nitrate (Supporting Information S1): Based on the initial changes in preformed NO_3 within the endmember regions we expect a global mean N^* increase of $\sim 5\%$ in the Perturbed experiment relative to the Control, once these anomalies have propagated through the deep ocean. Applying the sensitivity of atmospheric CO_2 to global

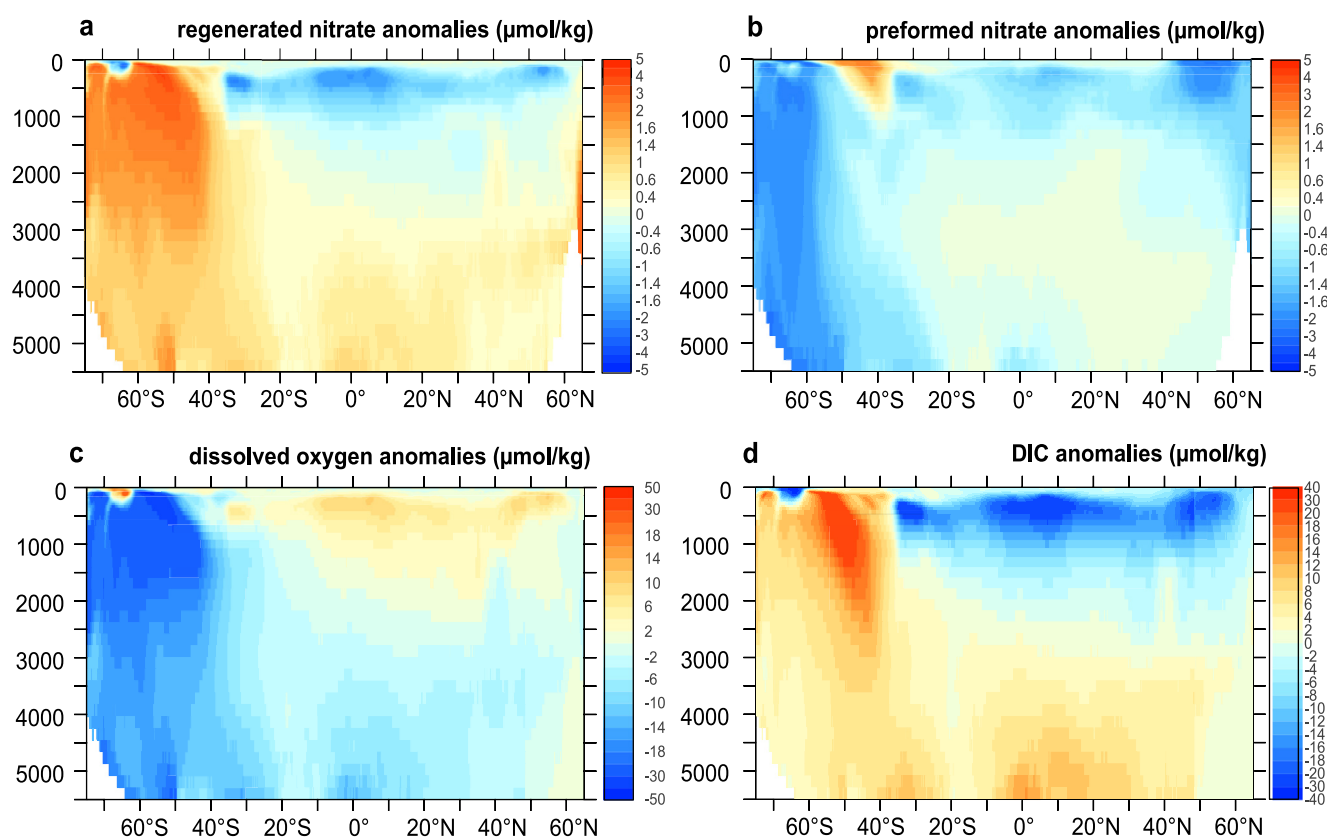


Figure 12. MOM5-SIS-Wombat biogeochemical results. Zonally averaged anomalies for Perturbed-Control in (a) regenerated NO_3 (mmol m^{-3}), (b) preformed NO_3 (mmol m^{-3}), (c) O_2 (mmol m^{-3}), and (d) DIC (mmol m^{-3}). Shown quantities are averaged over years 116–125 of each experiment.

preformed nutrients of Ito & Follows (2005), this increase in N^* within the Perturbed experiment equates to a long-term atmospheric CO_2 decrease of ~ 15 ppm. However, timeseries of the endmember preformed NO_3 values indicate they are not yet equilibrated and are still decreasing after 125 years such that this likely represents a conservative estimate of the increase in N^* and associated lowering of CO_2 we would expect if the Perturbed experiment was run to equilibrium.

The implications of our reconstructed wind changes on atmospheric CO_2 are likely to reach beyond the 15 ppm CO_2 drawdown suggested by the endmember preformed nutrient changes in the perturbation experiment. First, the LGM-Holocene wind shift we observe is 4.8° (rather than the 4° forcing applied to the model), suggesting the LGM CO_2 drawdown from wind shift is likely to be higher. If we assume a linear scaling between wind shift and the preformed nutrient changes described above, this would imply ~ 18 ppm CO_2 drawdown from the impact of wind shift on preformed nutrients at the LGM. Furthermore, we also reconstruct a 25% reduction in the wind strength that is not accounted for in the perturbation experiment. Earth System Models almost universally suggest increased CO_2 uptake from reduced wind strength (Gottschalk et al., 2019; Lauderdale et al., 2017), although the exact sensitivity of CO_2 to wind strength is poorly constrained, and depends somewhat on model resolution (Gottschalk et al., 2019). Applying the scaling of ~ 4 ppm CO_2 per 10% change in wind strength from a large compilation of model simulations (Gottschalk et al., 2019), the 25% reduction in the wind strength suggests a further CO_2 decrease of around 10 ppm. If the impacts of wind shift and strength were additive, this would take the combined impact of the reconstructed changes in wind shift and wind strength to ~ 28 ppm, without considering the impacts of nutrient “deepening” on the CaCO_3 cycle.

In addition to the reduction in endmember preformed nutrient concentrations, the model indicates a redistribution of the regenerated nutrient and carbon pools from intermediate depths toward the deep ocean, increasing the vertical carbon gradient with equatorward shifted winds (“nutrient deepening”; Figure 12). The deepening of the regenerated nutrient and carbon pools would drive a further CO_2 decrease via carbonate compensation (Boyle, 1988b; Toggweiler, 1999). While the scaling between preformed nutrients and atmospheric CO_2

used above (Boyle, 1988a, 1988b) accounts for a linear approximation of CaCO_3 dissolution following the total increase in regenerated carbon within the ocean, the effect of nutrient deepening is not accounted for. Based on the initial changes we see in deep ocean Dissolved Inorganic Carbon (DIC) in the model (Figure 12d), and the scaling between intermediate-deep DIC and atmospheric CO_2 given in, we would thus expect a further substantial long-term decrease in CO_2 , in addition to that implied by the preformed nutrient changes described above (Boyle, 1988a, 1988b). Thus, our “best guess” at the total impact of our reconstructed changes in LGM winds on atmospheric CO_2 is upwards of ~ 30 ppm, broadly similar to the magnitude proposed from changes in solubility (Sigman & Boyle, 2000) and sea-ice (Marzocchi & Jansen, 2019).

3.8. Proxy Comparison and Overturning Dynamics

The sign of the simulated circulation and carbon cycle changes in response to an equatorward shift in the westerlies concur with proxy observations from the LGM of a more sluggish deep ocean circulation (Du et al., 2020; Rafter et al., 2022), an increase in regenerated nutrients and carbon within the deep ocean and a redistribution of regenerated nutrients and carbon toward the deep ocean (Anderson et al., 2019; Hoogakker et al., 2018; Jaccard & Galbraith, 2012; Peterson & Lisiecki, 2018; Rae et al., 2018), as well as with a shoaling of the AMOC (Figure 11; Gherardi et al., 2009). The simulated decrease in nutrient upwelling and export production within the polar Southern Ocean, and the increases further north, are also in good agreement with LGM proxy data (Figure 10; Jaccard et al., 2013; Kohfeld et al., 2013; Sigman & Boyle, 2000). While our wind-shift experiment simulates a reduction in deep ocean oxygen, in good agreement with the LGM proxy data (Figures 11 and 12; Anderson et al., 2019; Hoogakker et al., 2018; Jaccard & Galbraith, 2012), we emphasize that current-generation Earth System Models showing increased oceanic carbon storage under glacial forcings via the disequilibrium pump do not simulate this reduction in deep ocean oxygen (Eggleston & Galbraith, 2018; Galbraith & de Lavergne, 2019).

The sign of the simulated trends highlighted above is unlikely to be contingent on the limitations of the experimental design, which nevertheless should be emphasized: First, the perturbation is applied abruptly to the modern state, and is held only over 125 years. Second, buoyancy forcing only partially adjusts to the changing winds since atmospheric temperatures and precipitation remain unperturbed. Third, the simulated response may depend partly on parameterizations of eddy effects and vertical mixing. Despite these limitations, the simulated overturning trends are qualitatively consistent with expectations from theory (Toggweiler & Samuels, 1995) and realistic eddy-rich models (Bishop et al., 2016; Dufour et al., 2015; Section 2.4; Figure S7 in Supporting Information S1). The decline of the overturning rate below 2 km depth can be explained by the influence of bathymetry on the vertical extent of wind-driven upwelling (Bishop et al., 2016; Toggweiler & Samuels, 1995). Specifically, the presence of a zonally continuous channel above 2 km depth at Drake Passage latitudes ($56\text{--}60^\circ\text{S}$) favors deeper waters as the mass replacement for the surface divergence to its south (Dufour et al., 2015; Toggweiler & Samuels, 1995). Displacement of the Ekman divergence from south of 60°S to lower latitudes thus suppresses this privileged upwelling pathway of deepwaters (Bishop et al., 2016; Dufour et al., 2015; Toggweiler et al., 2006). Hence, we posit that the simulated slowdown of overturning deeper than 2 km is a consequence of its bathymetry-driven sensitivity to Ekman transport in the polar Southern Ocean.

This sensitivity to Ekman divergence in the polar Southern Ocean suggests that as the winds shifted poleward through the deglaciation, their ability to lift deepwaters to the surface would have increased in tandem with the northward Ekman transport at 60°S . To calculate changes in zonal wind stress at 60°S ($\tau_{u,60\text{S}}$) we use the emergent relationship between the wind latitude and the zonal-mean zonal wind stress at 60°S in the model ensemble (Figure 3c) and apply this relationship to our reconstruction of $\Delta\text{Lat}_{\text{wind}}$, propagating the uncertainties by Monte-Carlo simulation; the ensemble shows that the wind latitude is a better predictor of wind stress at 60°S ($R^2 = 0.9$; Figure 3c) than is the wind strength ($R^2 = 0.7$). We assume mid-Holocene wind stress equal to the modern climatology (0.09 N m^{-2} ; Figure 7c). We then calculate northward Ekman transport at 60°S (Figure 7d) as the zonal integral of $\tau_{u,60\text{S}}/(\rho_0 * f)$, where ρ_0 is the density of seawater ($1,027 \text{ kg m}^{-3}$), and f is the Coriolis parameter. The resultant time series of Ekman transport increases from a minimum of around 4 Sv during the LGM to around 14 Sv by the mid-Holocene (Figure 7d; the reconstruction of $\tau_{u,60\text{S}}$ and northward Ekman transport at 60°S is provided in Table S3). The resultant invigoration of deep-ocean overturning over deglaciation (Du et al., 2020; Rafter et al., 2022; Figure 13) would have driven carbon out of the deep-ocean into the upper-ocean and atmosphere. This concurs with records of deep Pacific oxygen (Hoogakker et al., 2018) and deep Southern Ocean pH (Rae et al., 2018), which suggest a loss of regenerated nutrients

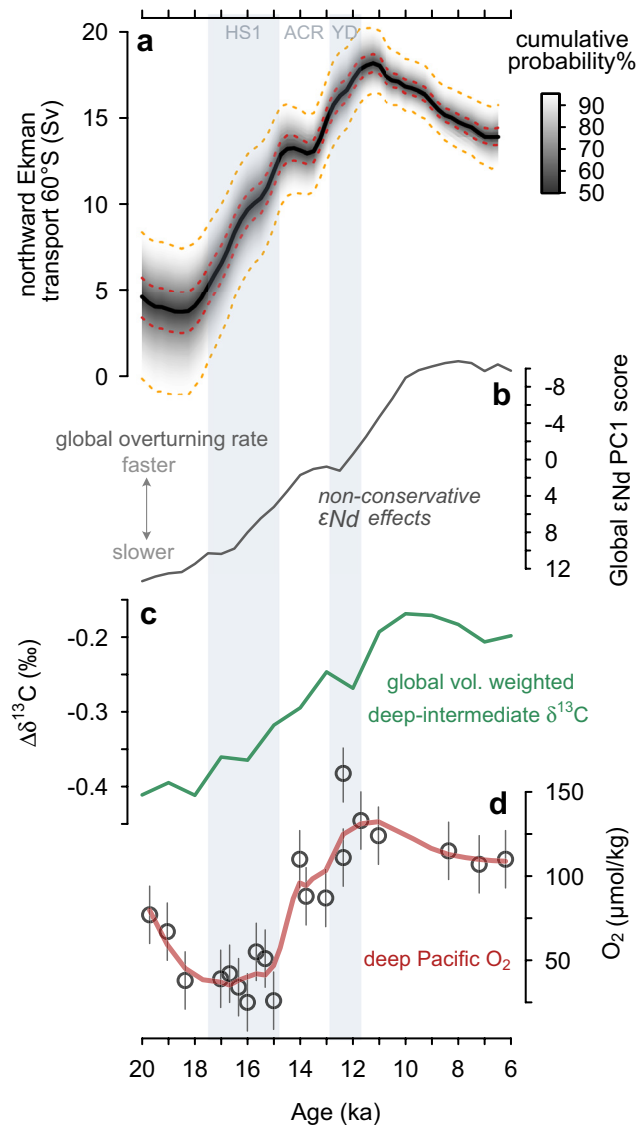


Figure 13. Deglacial changes in northward Ekman transport at 60°S with deep ocean overturning and carbon cycling. (a) Reconstructed change in northward Ekman transport at 60°S over deglaciation (lines show the 5th, 32nd, 50th, 68th, and 95th percentiles). (b) First principle component of global ϵNd data, representing non-conservative effects on ϵNd (Du et al., 2020). (c) Global volume-weighted deep-intermediate $\delta^{13}\text{C}$ gradient (Peterson & Lisiecki, 2018). (d) O_2 in the deep Pacific (Hoogakker et al., 2018) (fit with a LOESS smooth).

and carbon from the deep ocean over deglaciation (Figure 13). Furthermore, a decrease in the global-mean deep-intermediate carbon isotope gradient (Peterson & Lisiecki, 2018; Figure 13), and other carbon cycle tracers (Burke & Robinson, 2012; Hoogakker et al., 2018; Rae et al., 2018; Rafter et al., 2022), support a weakening of the vertical carbon gradient over deglaciation (Figure 13). Finally, records of nutrient utilization (Ai et al., 2020) and export production (Anderson et al., 2009) indicate an increase in nutrient upwelling to the Southern Ocean surface over deglaciation, with boron isotope records (Martínez-Botí et al., 2015) demonstrating a concurrent increase in CO_2 outgassing.

4. Conclusion

We use new and compiled planktic foraminiferal $\delta^{18}\text{O}$ from across the Southern Ocean and emergent relationships between SST front latitude, wind latitude, wind strength, and zonal wind stress at 60°S within an ensemble of climate models to reconstruct changes in the surface westerlies over the last deglaciation. We infer a 4.8° (2.9–7.1°, 95% CI) equatorward shift and a ~25% weakening of the westerlies during the LGM relative to the mid-Holocene. The reconstructed poleward shift in the westerlies over deglaciation is highly correlated with the rise in atmospheric CO_2 ($R^2 = 0.98$). We perform new experiments with a 0.25° resolution ocean-sea-ice-carbon model which indicate that shifting the westerlies equatorward increases oceanic carbon storage.

Our findings support the hypothesis that shifts in the Southern Hemisphere westerlies played a role in driving the deglacial rise in atmospheric CO_2 (Menviel et al., 2018), and thus may be an important mechanism (Sigman & Boyle, 2000; Toggweiler et al., 2006)—alongside changes in solubility (Sigman & Boyle, 2000) and Antarctic sea ice (Marzocchi & Jansen, 2019)—underlying glacial-interglacial CO_2 variations. Given that atmospheric CO_2 and global temperature can also influence the latitude of the westerlies (Chen et al., 2008; Yin, 2005), a deglacial feedback mechanism has been proposed (Toggweiler et al., 2006). The apparent temporal lead of shifts in the westerlies over atmospheric CO_2 and global temperature suggests that some initial change in the winds, perhaps driven by obliquity (Ai et al., 2020; Fogwill et al., 2015), could have initiated a cascade of increasing CO_2 , global warming, and poleward shifting winds. The tight coupling we infer between westerly wind latitude and atmospheric CO_2 over the last deglaciation, together with the sensitivity of the overturning circulation and carbon cycle to westerly wind latitude in our model experiments, suggest that future poleward shifts in the westerly winds (Chen et al., 2008; Yin, 2005) may drive a positive feedback on anthropogenic warming through a decrease in the efficiency of the biological pump and an increase in natural CO_2 outgassing from the Southern Ocean (Menviel et al., 2023).

Data Availability Statement

The new and compiled $\delta^{18}\text{O}$ data are given in table Table S1 and are available at Gray (2023b). The R code and data used to perform the $\Delta\text{Lat}_{\text{SST}}$ analysis is provided at Gray (2023a). The SST front and westerly wind reconstructions generated in this study ($\Delta\text{Lat}_{\text{SST}}$, $\Delta\text{Lat}_{\text{wind}}$, wind strength, zonal-mean zonal-wind stress at 60°S [$\tau_{u,60S}$], northward Ekman transport at 60°S) are given in Tables S2 and S3. The PMIP and CMIP data are available from <https://esgf-node.llnl.gov/projects/esgf-llnl/>. The results of the MOM5/SIS/WOMBAT experiment as shown in Figures 9–11 and Figures S6–S8 in Supporting Information S1 are available at Menviel & Spence (2021).

Acknowledgments

Some of the collaborations in this study were initiated through the PAGES QUIGS workshop 2020. EM received financial support from French-Swiss project VR-349-2012-6278 and CNRS-INSU project INDIEN-SUD. RCJW acknowledges funding from the U.S. National Science Foundation (Grant AGS-1929775). LM acknowledges funding from Australian Research Council Grant FT180100606. PS was supported by the Australian Research Council Grant FT190100413 and the Australian National Computing Infrastructure. MH acknowledges funding from Australian Research Council Grant DP210101650. We acknowledge the World Climate Research Programme, which, through its Working Group on Coupled Modelling, coordinated and promoted CMIP6, as well as the Working Group on Climate Models (WGCM) and Past Global Changes (PAGES) for their support of the Paleoclimate Modelling Intercomparison Project. We thank the climate modelling groups for producing and making available their model output, the Earth System Grid Federation (ESGF) for archiving the data and providing access, and the multiple funding agencies who support CMIP6 and ESGF. We thank the seven anonymous reviewers who provided helpful comments on previous versions of this manuscript, and the Editors for their input and guidance.

References

- Abernathy, R., Marshall, J., & Ferreira, D. (2011). The dependence of Southern Ocean meridional overturning on wind stress. *Journal of Physical Oceanography*, 41(12), 2261–2278. <https://doi.org/10.1175/JPO-D-11-023.1>
- Ai, X. E., Studer, A. S., Sigman, D. M., Martínez-García, A., Fripiat, F., Thöle, L. M., et al. (2020). Southern Ocean upwelling, Earth's obliquity, and glacial-interglacial atmospheric CO₂ change. *Science*, 370(6522), 1348–1352. <https://doi.org/10.1126/science.abd2115>
- Anderson, R. F., Ali, S., Bradtmiller, L. I., Nielsen, S. H. H., Fleisher, M. Q., Anderson, B. E., & Burckle, L. H. (2009). Wind-driven upwelling in the southern ocean and the deglacial rise in atmospheric CO₂. *Science*, 323(5920), 1443–1448. <https://doi.org/10.1126/science.1167441>
- Anderson, R. F., Sachs, J. P., Fleisher, M. Q., Allen, K. A., Yu, J., Koutavas, A., & Jaccard, S. L. (2019). Deep-sea oxygen depletion and ocean carbon sequestration during the last ice age. *Global Biogeochemical Cycles*, 33(3), 301–317. <https://doi.org/10.1029/2018GB006049>
- Annan, J. D., Hargreaves, J. C., & Mairitsen, T. (2022). A new global surface temperature reconstruction for the Last Glacial Maximum. *Climate of the Past*, 18(8), 1883–1896. <https://doi.org/10.5194/cp-18-1883-2022>
- Barnes, E. A., & Polvani, L. (2013). Response of the midlatitude jets, and of their variability, to increased greenhouse gases in the CMIP5 models. *Journal of Climate*, 26(18), 7117–7135. <https://doi.org/10.1175/JCLI-D-12-00536.1>
- Bishop, S. P., Gent, P. R., Bryan, F. O., Thompson, A. F., Long, M. C., & Abernathy, R. (2016). Southern ocean overturning compensation in an eddy-resolving climate simulation. *Journal of Physical Oceanography*, 46(5), 1575–1592. <https://doi.org/10.1175/JPO-D-15-0177.1>
- Bostock, H. C., Hayward, B. W., Neil, H. L., Sabaa, A. T., & Scott, G. H. (2015). Changes in the position of the Subtropical Front south of New Zealand since the last glacial period. *Paleoceanography*, 30(7), 824–844. <https://doi.org/10.1002/2014PA002652>
- Bostock, H. C., Opdyke, B. N., Gagan, M. K., & Fifield, L. K. (2004). Carbon isotope evidence for changes in Antarctic Intermediate Water circulation and ocean ventilation in the southwest Pacific during the last deglaciation. *Paleoceanography*, 19(4). <https://doi.org/10.1029/2004PA001047>
- Boyle, E. A. (1988a). The role of vertical chemical fractionation in controlling late Quaternary atmospheric carbon dioxide. *Journal of Geophysical Research*, 93(C12), 15701–15714. <https://doi.org/10.1029/JC093C12p15701>
- Boyle, E. A. (1988b). Vertical oceanic nutrient fractionation and glacial/interglacial CO₂ cycles. *Nature*, 331(6151), 55–56. Article 6151. <https://doi.org/10.1038/331055a0>
- Braconnot, P., Harrison, S. P., Kageyama, M., Bartlein, P. J., Masson-Delmotte, V., Abe-Ouchi, A., et al. (2012). Evaluation of climate models using palaeoclimatic data. *Nature Climate Change*, 2(6), 417–424. Article 6. <https://doi.org/10.1038/nclimate1456>
- Buizert, C., Sigl, M., Severi, M., Markle, B. R., Wettstein, J. J., McConnell, J. R., et al. (2018). Abrupt ice-age shifts in southern westerly winds and Antarctic climate forced from the north. *Nature*, 563(7733), 681–685. Article 7733. <https://doi.org/10.1038/s41586-018-0727-5>
- Burke, A., & Robinson, L. F. (2012). The southern ocean's role in carbon exchange during the last deglaciation. *Science*, 335(6068), 557–561. <https://doi.org/10.1126/science.1208163>
- Caley, T., Kim, J.-H., Malaizé, B., Giraudeau, J., Laepple, T., Caillon, N., et al. (2011). High-latitude obliquity as a dominant forcing in the Agulhas current system. *Climate of the Past*, 7(4), 1285–1296. <https://doi.org/10.5194/cp-7-1285-2011>
- Calvo, E., Pelejero, C., Deckker, P. D., & Logan, G. A. (2007). Antarctic deglacial pattern in a 30 Kyr record of sea surface temperature offshore South Australia. *Geophysical Research Letters*, 34(13), L13707. <https://doi.org/10.1029/2007GL029937>
- Caniupán, M., Lamy, F., Lange, C. B., Kaiser, J., Arz, H., Kilian, R., et al. (2011). Millennial-scale sea surface temperature and Patagonian Ice Sheet changes off southernmost Chile (53°S) over the past ~60 Kyr. *Paleoceanography*, 26(3). <https://doi.org/10.1029/2010PA002049>
- Carlson, A. E., Oppo, D. W., Came, R. E., LeGrande, A. N., Keigwin, L. D., & Curry, W. B. (2008). Subtropical Atlantic salinity variability and Atlantic meridional circulation during the last deglaciation. *Geology*, 36(12), 991–994. <https://doi.org/10.1130/G25080A.1>
- Chapman, C. C., Lea, M.-A., Meyer, A., Sallée, J.-B., & Hindell, M. (2020). Defining Southern Ocean fronts and their influence on biological and physical processes in a changing climate. *Nature Climate Change*, 10(3), 209–219. Article 3. <https://doi.org/10.1038/s41558-020-0705-4>
- Charles, C. D., Froelich, P. N., Zibello, M. A., Mortlock, R. A., & Morley, J. J. (1991). Biogenic opal in Southern Ocean sediments over the last 450,000 years: Implications for surface water chemistry and circulation. *Paleoceanography*, 6(6), 697–728. <https://doi.org/10.1029/91PA02477>
- Chavaillaz, Y., Codron, F., & Kageyama, M. (2013). Southern westerlies in LGM and future (RCP4.5) climates. *Climate of the Past*, 9(2), 517–524. <https://doi.org/10.5194/cp-9-517-2013>
- Chen, G., Lu, J., & Frierson, D. M. W. (2008). Phase speed spectra and the latitude of surface westerlies: Interannual variability and global warming trend. *Journal of Climate*, 21(22), 5942–5959. <https://doi.org/10.1175/2008JCLI2306.1>
- Chiessi, C. M., Mulitza, S., Groeneweld, J., Silva, J. B., Campos, M. C., & Gurgel, M. H. C. (2014). Variability of the Brazil Current during the late Holocene. *Palaeogeography, Palaeoclimatology, Palaeoecology*, 415, 28–36. <https://doi.org/10.1016/j.palaeo.2013.12.005>
- Crosta, X., Sturm, A., Armand, L., & Pichon, J.-J. (2004). Late Quaternary sea ice history in the Indian sector of the Southern Ocean as recorded by diatom assemblages. *Marine Micropaleontology*, 50(3), 209–223. [https://doi.org/10.1016/S0377-8398\(03\)00072-0](https://doi.org/10.1016/S0377-8398(03)00072-0)
- Dong, S., Sprintall, J., & Gille, S. T. (2006). Location of the Antarctic polar front from AMSR-E satellite sea surface temperature measurements. *Journal of Physical Oceanography*, 36(11), 2075–2089. <https://doi.org/10.1175/JPO2973.1>
- Downes, S. M., & Hogg, A. M. C. (2013). Southern Ocean circulation and eddy compensation in CMIP5 models. *Journal of Climate*, 26(18), 7198–7220. <https://doi.org/10.1175/JCLI-D-12-00504.1>
- Du, J., Haley, B. A., & Mix, A. C. (2020). Evolution of the global overturning circulation since the Last Glacial Maximum based on marine authigenic neodymium isotopes. *Quaternary Science Reviews*, 241, 106396. <https://doi.org/10.1016/j.quascirev.2020.106396>
- Dufour, C. O., Griffies, S. M., de Souza, G. F., Frenger, I., Morrison, A. K., Palter, J. B., et al. (2015). Role of mesoscale eddies in cross-frontal transport of heat and biogeochemical tracers in the Southern Ocean. *Journal of Physical Oceanography*, 45(12), 3057–3081. <https://doi.org/10.1175/JPO-D-14-0240.1>
- Dufour, C. O., Le Sommer, J., Zika, J. D., Gehlen, M., Orr, J. C., Mathiot, P., & Barnier, B. (2012). Standing and transient eddies in the response of the Southern Ocean meridional overturning to the southern annular mode. *Journal of Climate*, 25(20), 6958–6974. <https://doi.org/10.1175/JCLI-D-11-00309.1>
- Dyez, K. A., Zahn, R., & Hall, I. R. (2014). Multicentennial Agulhas leakage variability and links to North Atlantic climate during the past 80,000 years. *Paleoceanography*, 29(12), 1238–1248. <https://doi.org/10.1002/2014PA002698>
- Efron, B. (1979). Bootstrap methods: Another look at the jackknife. *Annals of Statistics*, 7(1), 1–26. <https://doi.org/10.1214/aos/1176344552>
- Eggleston, S., & Galbraith, E. D. (2018). The devil's in the disequilibrium: Multi-component analysis of dissolved carbon and oxygen changes under a broad range of forcings in a general circulation model. *Biogeosciences*, 15(12), 3761–3777. <https://doi.org/10.5194/bg-15-3761-2018>
- Eyring, V., Bony, S., Meehl, G. A., Senior, C. A., Stevens, B., Stouffer, R. J., & Taylor, K. E. (2016). Overview of the Coupled Model Intercomparison Project Phase 6 (CMIP6) experimental design and organization. *Geoscientific Model Development*, 9(5), 1937–1958. <https://doi.org/10.5194/gmd-9-1937-2016>

- Eyring, V., Cox, P. M., Flato, G. M., Gleckler, P. J., Abramowitz, G., Caldwell, P., et al. (2019). Taking climate model evaluation to the next level. *Nature Climate Change*, 9(2), 102–110. <https://doi.org/10.1038/s41558-018-0355-y>
- Fathrio, I., Iizuka, S., Manda, A., Kodama, Y.-M., Ishida, S., Moteki, Q., et al. (2017). Assessment of western Indian Ocean SST bias of CMIP5 models. *Journal of Geophysical Research: Oceans*, 122(4), 3123–3140. <https://doi.org/10.1002/2016JC012443>
- Fischer, G., & Wefer, G. (Eds.). (1999). *Use of proxies in paleoceanography: Examples from the South Atlantic*. Springer-Verlag. <https://doi.org/10.1007/978-3-642-58646-0>
- Fogwill, C. J., Turney, C. S. M., Hutchinson, D. K., Taschetto, A. S., & England, M. H. (2015). Obliquity control on southern hemisphere climate during the last glacial. *Scientific Reports*, 5(1), 11673. Article 1. <https://doi.org/10.1038/srep11673>
- Galbraith, E., & de Lavergne, C. (2019). Response of a comprehensive climate model to a broad range of external forcings: Relevance for deep ocean ventilation and the development of late Cenozoic ice ages. *Climate Dynamics*, 52(1), 653–679. <https://doi.org/10.1007/s00382-018-4157-8>
- Gent, P. R. (2016). Effects of southern hemisphere wind changes on the meridional overturning circulation in ocean models. *Annual Review of Marine Science*, 8(1), 79–94. <https://doi.org/10.1146/annurev-marine-122414-033929>
- Gent, P. R., & McWilliams, J. C. (1990). Isopycnal mixing in ocean circulation models. *Journal of Physical Oceanography*, 20(1), 150–155. [https://doi.org/10.1175/1520-0485\(1990\)020<0150:IMOCM>2.0.CO;2](https://doi.org/10.1175/1520-0485(1990)020<0150:IMOCM>2.0.CO;2)
- Gersonde, R., Hodell, D. A., & Blum, P. (Eds.). (2003). *Proceedings of the ocean drilling program, 177 scientific results* (Vol. 177). Ocean Drilling Program. <https://doi.org/10.2973/odp.proc.sr.177.2003>
- Gherardi, J.-M., Labeyrie, L., Nave, S., Francois, R., McManus, J. F., & Cortijo, E. (2009). Glacial-interglacial circulation changes inferred from $^{231}\text{Pa}/^{230}\text{Th}$ sedimentary record in the North Atlantic region. *Paleoceanography*, 24(2). <https://doi.org/10.1029/2008PA001696>
- Gottschalk, J., Battaglia, G., Fischer, H., Frölicher, T. L., Jaccard, S. L., Jeltsch-Thömmes, A., et al. (2019). Mechanisms of millennial-scale atmospheric CO_2 change in numerical model simulations. *Quaternary Science Reviews*, 220, 30–74. <https://doi.org/10.1016/j.quascirev.2019.05.013>
- Gottschalk, J., Hodell, D. A., Skinner, L. C., Crowhurst, S. J., Jaccard, S. L., & Charles, C. (2018). Past carbonate preservation events in the deep southeast Atlantic ocean (Cape Basin) and their implications for Atlantic overturning dynamics and marine carbon cycling. *Paleoceanography and Paleoclimatology*, 33(6), 643–663. <https://doi.org/10.1029/2018PA003353>
- Gottschalk, J., Michel, E., Thöle, L. M., Studer, A. S., Hasenfratz, A. P., Schmid, N., et al. (2020). Glacial heterogeneity in Southern Ocean carbon storage abated by fast South Indian deglacial carbon release. *Nature Communications*, 11(1), 6192. Article 1. <https://doi.org/10.1038/s41467-020-20034-1>
- Gottschalk, J., Skinner, L. C., & Waelbroeck, C. (2015). Contribution of seasonal sub-Antarctic surface water variability to millennial-scale changes in atmospheric CO_2 over the last deglaciation and Marine Isotope Stage 3. *Earth and Planetary Science Letters*, 411, 87–99. <https://doi.org/10.1016/j.epsl.2014.11.051>
- Govin, A., Michel, E., Labeyrie, L., Waelbroeck, C., Dewilde, F., & Jansen, E. (2009). Evidence for northward expansion of Antarctic Bottom Water mass in the Southern Ocean during the last glacial inception. *Paleoceanography*, 24(1). <https://doi.org/10.1029/2008PA001603>
- Gray, W. (2023a). willyrgray/SOD180: SOD180_v1.1 (SOD180_v1.1). [Software]. Zenodo. <https://doi.org/10.5281/zenodo.7866501>
- Gray, W. R. (2023b). Compilation of deglacial Southern Ocean planktic foraminiferal $\delta^{18}\text{O}$ data [Dataset]. PANGAEA. <https://doi.org/10.1594/PANGAEA.932846>
- Gray, W. R., Wills, R. C. J., Rae, J. W. B., Burke, A., Ivanovic, R. F., Roberts, W. H. G., et al. (2020). Wind-driven evolution of the North Pacific subpolar gyre over the last deglaciation. *Geophysical Research Letters*, 47(6), e2019GL086328. <https://doi.org/10.1029/2019GL086328>
- Griffies, S. M., Biastoch, A., Böning, C., Bryan, F., Danabasoglu, G., Chassignet, E. P., et al. (2009). Coordinated ocean-ice reference experiments (COREs). *Ocean Modelling*, 26(1), 1–46. <https://doi.org/10.1016/j.ocemod.2008.08.007>
- Grobe, H., & Mackensen, A. (1992). Late Quaternary climatic cycles as recorded in sediments from the Antarctic continental margin. In J. P. Kennett, & D. A. Warkne (Eds.), *Antarctic Research series* (Vol. 56, pp. 349–376). American Geophysical Union. <https://doi.org/10.1029/AR056p0349>
- Haddam, N. A., Michel, E., Siani, G., Licari, L., & Dewilde, F. (2020). Ventilation and expansion of intermediate and deep waters in the southeast Pacific during the last termination. *Paleoceanography and Paleoclimatology*, 35(7), e2019PA003743. <https://doi.org/10.1029/2019PA003743>
- Haddam, N. A., Siani, G., Michel, E., Kaiser, J., Lamy, F., Duchamp-Alphonse, S., et al. (2018). Changes in latitudinal sea surface temperature gradients along the Southern Chilean margin since the last glacial. *Quaternary Science Reviews*, 194, 62–76. <https://doi.org/10.1016/j.quascirev.2018.06.023>
- Hall, A., Cox, P., Huntingford, C., & Klein, S. (2019). Progressing emergent constraints on future climate change. *Nature Climate Change*, 9(4), 269–278. <https://doi.org/10.1038/s41558-019-0436-6>
- Hallberg, R., & Gnanadesikan, A. (2006). The role of eddies in determining the structure and response of the wind-driven southern hemisphere overturning: Results from the modeling eddies in the Southern Ocean (MESO) project. *Journal of Physical Oceanography*, 36(12), 2232–2252. <https://doi.org/10.1175/JPO2980.1>
- Hasenfratz, A. P., Jaccard, S. L., Martínez-García, A., Sigman, D. M., Hodell, D. A., Vance, D., et al. (2019). The residence time of Southern Ocean surface waters and the 100,000-year ice age cycle. *Science*, 363(6431), 1080–1084. <https://doi.org/10.1126/science.aat7067>
- Hodell, D. A., Charles, C. D., & Ninnemann, U. S. (2000). Comparison of interglacial stages in the South Atlantic sector of the southern ocean for the past 450 Kyr: Implications for Marine Isotope Stage (MIS) 11. *Global and Planetary Change*, 24(1), 7–26. [https://doi.org/10.1016/S0921-8181\(99\)00069-7](https://doi.org/10.1016/S0921-8181(99)00069-7)
- Hodell, D. A., Venz, K. A., Charles, C. D., & Ninnemann, U. S. (2003). Pleistocene vertical carbon isotope and carbonate gradients in the South Atlantic sector of the Southern Ocean. *Geochemistry, Geophysics, Geosystems*, 4(1), 1–19. <https://doi.org/10.1029/2002GC000367>
- Hogg, A. M., Spence, P., Saenko, O. A., & Downes, S. M. (2017). The energetics of Southern Ocean upwelling. *Journal of Physical Oceanography*, 47(1), 135–153. <https://doi.org/10.1175/JPO-D-16-0176.1>
- Hoogakker, B. A. A., Lu, Z., Umling, N., Jones, L., Zhou, X., Rickaby, R. E. M., et al. (2018). Glacial expansion of oxygen-depleted seawater in the eastern tropical Pacific. *Nature*, 562(7727), 410–413. Article 7727. <https://doi.org/10.1038/s41586-018-0589-x>
- Ito, T., & Follows, M. J. (2005). Preformed phosphate, soft tissue pump and atmospheric CO_2 . *Journal of Marine Research*, 63(4), 813–839. <https://doi.org/10.1357/0022240054663231>
- Jaccard, S. L., & Galbraith, E. D. (2012). Large climate-driven changes of oceanic oxygen concentrations during the last deglaciation. *Nature Geoscience*, 5(2), 151–156. Article 2. <https://doi.org/10.1038/ngeo1352>
- Jaccard, S. L., Hayes, C. T., Martínez-García, A., Hodell, D. A., Anderson, R. F., Sigman, D. M., & Haug, G. H. (2013). Two modes of change in Southern Ocean productivity over the past million years. *Science*, 339(6126), 1419–1423. <https://doi.org/10.1126/science.1227545>
- Jackett, D., & McDougall, T. (1997). A neutral density variable for the world's oceans. [https://doi.org/10.1175/1520-0485\(1997\)027<0237:ANDVFT>2.0.CO;2](https://doi.org/10.1175/1520-0485(1997)027<0237:ANDVFT>2.0.CO;2)

- Kageyama, M., Braconnot, P., Harrison, S. P., Haywood, A. M., Jungclaus, J. H., Otto-Bliesner, B. L., et al. (2018). The PMIP4 contribution to CMIP6—Part 1: Overview and over-arching analysis plan. *Geoscientific Model Development*, 11(3), 1033–1057. <https://doi.org/10.5194/gmd-11-1033-2018>
- Kageyama, M., Harrison, S. P., Kapsch, M.-L., Löfverström, M., Lora, J. M., Mikolajewicz, U., et al. (2020). The PMIP4-CMIP6 Last Glacial Maximum experiments: Preliminary results and comparison with the PMIP3-CMIP5 simulations. *Climate of the Past Discussions*, 1–37. <https://doi.org/10.5194/cp-2019-169>
- Kim, S.-T., & O'Neil, J. R. (1997). Equilibrium and nonequilibrium oxygen isotope effects in synthetic carbonates. *Geochimica et Cosmochimica Acta*, 61(16), 3461–3475. [https://doi.org/10.1016/S0016-7037\(97\)00169-5](https://doi.org/10.1016/S0016-7037(97)00169-5)
- Kohfeld, K. E., Graham, R. M., de Boer, A. M., Sime, L. C., Wolff, E. W., Le Quéré, C., & Bopp, L. (2013). Southern Hemisphere westerly wind changes during the Last Glacial Maximum: Paleo-data synthesis. *Quaternary Science Reviews*, 68, 76–95. <https://doi.org/10.1016/j.quascirev.2013.01.017>
- Labeyrie, L., Labracherie, M., Gorfii, N., Pichon, J. J., Vautravers, M., Arnold, M., et al. (1996). Hydrographic changes of the Southern Ocean (southeast Indian Sector) over the last 230 Kyr. *Paleoceanography*, 11(1), 57–76. <https://doi.org/10.1029/95PA02255>
- Lambeck, K., Rouby, H., Purcell, A., Sun, Y., & Sambridge, M. (2014). Sea level and global ice volumes from the Last Glacial Maximum to the Holocene. *Proceedings of the National Academy of Sciences of the United States of America*, 111(43), 15296–15303. <https://doi.org/10.1073/pnas.1411762111>
- Lamy, F., Kaiser, J., Ninnemann, U., Hebbeln, D., Arz, H. W., & Stoner, J. (2004). Antarctic timing of surface water changes off Chile and Patagonian ice sheet response. *Science*, 304(5679), 1959–1962. <https://doi.org/10.1126/science.1097863>
- Lamy, F., Kilian, R., Arz, H. W., Francois, J.-P., Kaiser, J., Prange, M., & Steinke, T. (2010). Holocene changes in the position and intensity of the southern westerly wind belt. *Nature Geoscience*, 3(10), 695–699. <https://doi.org/10.1038/ngeo959>
- Lauderdale, J. M., Williams, R. G., Munday, D. R., & Marshall, D. P. (2017). The impact of Southern Ocean residual upwelling on atmospheric CO₂ on centennial and millennial timescales. *Climate Dynamics*, 48(5), 1611–1631. <https://doi.org/10.1007/s00382-016-3163-y>
- Levi, C., Labeyrie, L., Bassinot, F., Guichard, F., Cortijo, E., Waelbroeck, C., et al. (2007). Low-latitude hydrological cycle and rapid climate changes during the last deglaciation. *Geochemistry, Geophysics, Geosystems*, 8(5), Q05N12. <https://doi.org/10.1029/2006GC001514>
- Li, C., & Battisti, D. S. (2008). Reduced Atlantic storminess during Last Glacial Maximum: Evidence from a coupled climate model. *Journal of Climate*, 21(14), 3561–3579. <https://doi.org/10.1175/2007JCLI2166.1>
- Lu, Z., Hoogakker, B. A. A., Hillenbrand, C.-D., Zhou, X., Thomas, E., Gutchess, K. M., et al. (2016). Oxygen depletion recorded in upper waters of the glacial Southern Ocean. *Nature Communications*, 7(1), 11146. Article 1. <https://doi.org/10.1038/ncomms11146>
- Malevich, S. B., Vetter, L., & Tierney, J. E. (2019). Global core top calibration of $\delta^{18}\text{O}$ in planktic foraminifera to sea surface temperature. *Paleoceanography and Paleoclimatology*, 34(8), 1292–1315. <https://doi.org/10.1029/2019PA003576>
- Marcott, S. A., Bauska, T. K., Buizert, C., Steig, E. J., Rosen, J. L., Cuffey, K. M., et al. (2014). Centennial-scale changes in the global carbon cycle during the last deglaciation. *Nature*, 514(7524), 616–619. <https://doi.org/10.1038/nature13799>
- Marshall, J., & Speer, K. (2012). Closure of the meridional overturning circulation through Southern Ocean upwelling. *Nature Geoscience*, 5(3), 171–180. Article 3. <https://doi.org/10.1038/ngeo1391>
- Martin, J. H., Gordon, R. M., & Fitzwater, S. E. (1990). Iron in Antarctic waters. *Nature*, 345(6271), 156–158. Article 6271. <https://doi.org/10.1038/345156a0>
- Martínez-Botí, M. A., Marino, G., Foster, G. L., Ziveri, P., Henahan, M. J., Rae, J. W. B., et al. (2015). Boron isotope evidence for oceanic carbon dioxide leakage during the last deglaciation. *Nature*, 518(7538), 219–222. Article 7538. <https://doi.org/10.1038/nature14155>
- Martínez-Méndez, G., Zahn, R., Hall, I. R., Peeters, F. J. C., Pena, L. D., Cacho, I., & Negre, C. (2010). Contrasting multiproxy reconstructions of surface ocean hydrography in the Agulhas Corridor and implications for the Agulhas Leakage during the last 345,000 years. *Paleoceanography*, 25(4). <https://doi.org/10.1029/2009PA001879>
- Marzocchi, A., & Jansen, M. F. (2017). Connecting Antarctic sea ice to deep-ocean circulation in modern and glacial climate simulations. *Geophysical Research Letters*, 44(12), 6286–6295. <https://doi.org/10.1002/2017GL073936>
- Marzocchi, A., & Jansen, M. F. (2019). Global cooling linked to increased glacial carbon storage via changes in Antarctic sea ice. *Nature Geoscience*, 12(12), 1001–1005. Article 12. <https://doi.org/10.1038/s41561-019-0466-8>
- Mashiotta, T. A., Lea, D. W., & Spero, H. J. (1999). Glacial–interglacial changes in Subantarctic sea surface temperature and $\delta^{18}\text{O}$ -water using foraminiferal Mg. *Earth and Planetary Science Letters*, 170(4), 417–432. [https://doi.org/10.1016/S0012-821X\(99\)00116-8](https://doi.org/10.1016/S0012-821X(99)00116-8)
- Mazloff, M. R., Ferrari, R., & Schneider, T. (2013). The force balance of the Southern Ocean meridional overturning circulation. *Journal of Physical Oceanography*, 43(6), 1193–1208. <https://doi.org/10.1175/JPO-D-12-069.1>
- McGraw, M. C., & Barnes, E. A. (2016). Seasonal sensitivity of the eddy-driven jet to tropospheric heating in an idealized AGCM. *Journal of Climate*, 29(14), 5223–5240. <https://doi.org/10.1175/JCLI-D-15-0723.1>
- Menviel, L., & Spence, P. (2021). Impact of an equatorward shift of the SH westerlies on the carbon cycle [Dataset]. UNSWorks. <https://doi.org/10.26190/unsworks/1608>
- Menviel, L., Spence, P., Yu, J., Chamberlain, M. A., Matear, R. J., Meissner, K. J., & England, M. H. (2018). Southern Hemisphere westerlies as a driver of the early deglacial atmospheric CO₂ rise. *Nature Communications*, 9(1), 2503. Article 1. <https://doi.org/10.1038/s41467-018-04876-4>
- Menviel, L. C., Spence, P., Kiss, A. E., Chamberlain, M. A., Hayashida, H., England, M. H., & Waugh, D. (2023). Enhanced Southern Ocean CO₂ outgassing as a result of stronger and poleward shifted southern hemispheric westerlies. Biogeochemistry: Greenhouse Gases. [Preprint]. <https://doi.org/10.5194/egusphere-2023-390>
- Mitchell, B. G., Brody, E. A., Holm-Hansen, O., McClain, C., & Bishop, J. (1991). Light limitation of phytoplankton biomass and macronutrient utilization in the Southern Ocean. *Limnology & Oceanography*, 36(8), 1662–1677. <https://doi.org/10.4319/lo.1991.36.8.1662>
- Mohtadi, M., Rossel, P., Lange, C. B., Pantoja, S., Böning, P., Repeta, D. J., et al. (2008). Deglacial pattern of circulation and marine productivity in the upwelling region off central-south Chile. *Earth and Planetary Science Letters*, 272(1), 221–230. <https://doi.org/10.1016/j.epsl.2008.04.043>
- Nakamura, H., Sampe, T., Goto, A., Ohfuchi, W., & Xie, S.-P. (2008). On the importance of midlatitude oceanic frontal zones for the mean state and dominant variability in the tropospheric circulation. *Geophysical Research Letters*, 35(15), L15709. <https://doi.org/10.1029/2008GL034010>
- Nakamura, H., Sampe, T., Tanimoto, Y., & Shimpo, A. (2004). Observed associations among storm tracks, jet streams and midlatitude oceanic fronts. In C. Wang, S. P. Xie, & J. A. Carton (Eds.), *Geophysical monograph series* (pp. 329–345). American Geophysical Union. <https://doi.org/10.1029/147GM18>
- Nelson, C. S., Hendy, I. L., Neil, H. L., Hendy, C. H., & Weaver, P. P. E. (2000). Last glacial jetting of cold waters through the Subtropical Convergence zone in the Southwest Pacific off eastern New Zealand, and some geological implications. *Palaeogeography, Palaeoclimatology, Palaeoecology*, 156(1), 103–121. [https://doi.org/10.1016/S0031-0182\(99\)00134-0](https://doi.org/10.1016/S0031-0182(99)00134-0)

- Olsen, A., Key, R. M., van Heuven, S., Lauvset, S. K., Velo, A., Lin, X., et al. (2016). The global ocean data analysis project version 2 (GLODAPv2)—An internally consistent data product for the world ocean. *Earth System Science Data*, 8(2), 297–323. <https://doi.org/10.5194/essd-8-297-2016>
- Pasquier, B., & Holzer, M. (2016). The plumbing of the global biological pump: Efficiency control through leaks, pathways, and time scales. *Journal of Geophysical Research: Oceans*, 121(8), 6367–6388. <https://doi.org/10.1002/2016JC011821>
- Pereira, L. S., Arz, H. W., Pätzold, J., & Portillo-Ramos, R. C. (2018). Productivity evolution in the South Brazilian bight during the last 40,000 years. *Paleoceanography and Paleoclimatology*, 33(12), 1339–1356. <https://doi.org/10.1029/2018PA003406>
- Peterson, C. D., & Lisiecki, L. E. (2018). Deglacial carbon cycle changes observed in a compilation of 127 benthic $\delta^{13}\text{C}$ time series (20–6 ka). *Climate of the Past*, 14(8), 1229–1252. <https://doi.org/10.5194/cp-14-1229-2018>
- Pichon, J.-J., Labeyrie, L. D., Barette, G., Labracherie, M., Duprat, J., & Jouzel, J. (1992). Surface water temperature changes in the high latitudes of the southern hemisphere over the Last Glacial-Interglacial Cycle. *Paleoceanography*, 7(3), 289–318. <https://doi.org/10.1029/92PA00709>
- Portillo-Ramos, R. C., Cruz, A. P. S., Barbosa, C. F., Rathburn, A. E., Mulitza, S., Venancio, I. M., et al. (2018). Methane release from the southern Brazilian margin during the last glacial. *Scientific Reports*, 8(1), 5948. Article 1. <https://doi.org/10.1038/s41598-018-24420-0>
- Rae, J. W. B., Burke, A., Robinson, L. F., Adkins, J. F., Chen, T., Cole, C., et al. (2018). CO_2 storage and release in the deep Southern Ocean on millennial to centennial timescales. *Nature*, 562(7728), 569–573. Article 7728. <https://doi.org/10.1038/s41586-018-0614-0>
- Rafter, P. A., Gray, W. R., Hines, S. K. V., Burke, A., Costa, K. M., Gottschalk, J., et al. (2022). Global reorganization of deep-sea circulation and carbon storage after the last ice age. *Science Advances*, 8(46), eabq5434. <https://doi.org/10.1126/sciadv.abq5434>
- Redi, M. H. (1982). Oceanic isopycnal mixing by coordinate rotation. *Journal of Physical Oceanography*, 12(10), 1154–1158. [https://doi.org/10.1175/1520-0485\(1982\)012<1154:OIMBCR>2.0.CO;2](https://doi.org/10.1175/1520-0485(1982)012<1154:OIMBCR>2.0.CO;2)
- Rickaby, R. E. M., & Elderfield, H. (1999). Planktonic foraminiferal Cd/Ca: Paleonutrients or paleotemperature? *Paleoceanography*, 14(3), 293–303. <https://doi.org/10.1029/1999PA000007>
- Santos, T. P., Lessa, D. O., Venancio, I. M., Chiessi, C. M., Mulitza, S., Kuhnert, H., et al. (2017). Prolonged warming of the Brazil Current precedes deglaciations. *Earth and Planetary Science Letters*, 463, 1–12. <https://doi.org/10.1016/j.epsl.2017.01.014>
- Sarnthein, M., Winn, K., Jung, S. J. A., Duplessy, J.-C., Labeyrie, L., Erlenkeuser, H., & Ganssen, G. (1994). Changes in East Atlantic Deepwater Circulation over the last 30,000 years: Eight time slice reconstructions. *Paleoceanography*, 9(2), 209–267. <https://doi.org/10.1029/93PA03301>
- Saunders, K. M., Roberts, S. J., Perren, B., Butz, C., Sime, L., Davies, S., et al. (2018). Holocene dynamics of the Southern Hemisphere westerly winds and possible links to CO_2 outgassing. *Nature Geoscience*, 11(9), 650–655. Article 9. <https://doi.org/10.1038/s41561-018-0186-5>
- Schiraldi, B., Sikes, E. L., Elmore, A. C., Cook, M. S., & Rose, K. A. (2014). Southwest Pacific subtropics responded to last deglacial warming with changes in shallow water sources. *Paleoceanography*, 29(6), 595–611. <https://doi.org/10.1002/2013PA002584>
- Schneider, R. R., Müller, P. J., & Ruhland, G. (1995). Late Quaternary surface circulation in the east equatorial South Atlantic: Evidence from Alkenone sea surface temperatures. *Paleoceanography*, 10(2), 197–219. <https://doi.org/10.1029/94PA03308>
- Schrag, D. P., Adkins, J. F., McIntyre, K., Alexander, J. L., Hodell, D. A., Charles, C. D., & McManus, J. F. (2002). The oxygen isotopic composition of seawater during the Last Glacial Maximum. *Quaternary Science Reviews*, 21(1), 331–342. [https://doi.org/10.1016/S0277-3791\(01\)00110-X](https://doi.org/10.1016/S0277-3791(01)00110-X)
- Scussolini, P., & Peeters, F. J. C. (2013). A record of the last 460 thousand years of upper ocean stratification from the central Walvis Ridge, South Atlantic. *Paleoceanography*, 28(3), 426–439. <https://doi.org/10.1002/palo.20041>
- Shakun, J. D., Clark, P. U., He, F., Marcott, S. A., Mix, A. C., Liu, Z., et al. (2012). Global warming preceded by increasing carbon dioxide concentrations during the last deglaciation. *Nature*, 484(7392), 49–54. Article 7392. <https://doi.org/10.1038/nature10915>
- Siecre, M. A., Labeyrie, L., Ezat, U., Duprat, J., Turon, J. L., Schmidt, S., et al. (2005). Mid-latitude southern Indian Ocean response to northern hemisphere Heinrich events. *Earth and Planetary Science Letters*, 240(3), 724–731. <https://doi.org/10.1016/j.epsl.2005.09.032>
- Sigl, M., Fudge, T. J., Winstrup, M., Cole-Dai, J., Ferris, D., McConnell, J. R., et al. (2016). The WAIS divide deep ice core WD2014 chronology—Part 2: Annual-layer counting (0–31 ka BP). *Climate of the Past*, 12(3), 769–786. <https://doi.org/10.5194/cp-12-769-2016>
- Sigman, D. M., & Boyle, E. A. (2000). Glacial/interglacial variations in atmospheric carbon dioxide. *Nature*, 407(6806), 859–869. Article 6806. <https://doi.org/10.1038/35038000>
- Sikes, E. L., Howard, W. R., Samson, C. R., Mahan, T. S., Robertson, L. G., & Volkman, J. K. (2009). Southern Ocean seasonal temperature and Subtropical Front movement on the South Tasman Rise in the late Quaternary. *Paleoceanography*, 24(2). <https://doi.org/10.1029/2008PA001659>
- Siler, N., Roe, G. H., & Armour, K. C. (2018). Insights into the zonal-mean response of the hydrologic cycle to global warming from a diffusive energy balance model. *Journal of Climate*, 31(18), 7481–7493. <https://doi.org/10.1175/JCLI-D-18-0081.1>
- Sime, L. C., Hodgson, D., Bracegirdle, T. J., Allen, C., Perren, B., Roberts, S., & de Boer, A. M. (2016). Sea ice led to poleward-shifted winds at the Last Glacial Maximum: The influence of state dependency on CMIP5 and PMIP3 models. *Climate of the Past*, 12(12), 2241–2253. <https://doi.org/10.5194/cp-12-2241-2016>
- Sime, L. C., Kohfeld, K. E., Le Quéré, C., Wolff, E. W., de Boer, A. M., Graham, R. M., & Bopp, L. (2013). Southern Hemisphere westerly wind changes during the Last Glacial Maximum: Model-data comparison. *Quaternary Science Reviews*, 64, 104–120. <https://doi.org/10.1016/j.quascirev.2012.12.008>
- Simpson, G. L. (2018). Modelling palaeoecological time series using generalised additive models. *Frontiers in Ecology and Evolution*, 6. <https://doi.org/10.3389/fevo.2018.00149>
- Spence, P., Saenko, O. A., Eby, M., & Weaver, A. J. (2009). The Southern Ocean Overturning: Parameterized versus permitted eddies. *Journal of Physical Oceanography*, 39(7), 1634–1651. <https://doi.org/10.1175/2009JPO4120.1>
- Stewart, K. D., Hogg, A. M. C., England, M. H., Waugh, D. W., & Kiss, A. E. (2021). The Ekman streamfunction and the Eulerian and residual overturning circulations of the Southern Ocean. *Geophysical Research Letters*, 48(17). <https://doi.org/10.1029/2021GL093438>
- Stocker, T. F., & Johnsen, S. J. (2003). A minimum thermodynamic model for the bipolar seesaw. *Paleoceanography*, 18(4). <https://doi.org/10.1029/2003PA000920>
- Stuut, J.-B. W., Deckker, P. D., Saavedra-Pellitero, M., Bassinot, F., Drury, A. J., Walczak, M. H., et al. (2019). A 5.3-million-year history of monsoonal precipitation in northwestern Australia. *Geophysical Research Letters*, 46(12), 6946–6954. <https://doi.org/10.1029/2019GL083035>
- Stuut, J.-B. W., Prins, M. A., Schneider, R. R., Weltje, G. J., Jansen, J. H. F., & Postma, G. (2002). A 300-Kyr record of aridity and wind strength in southwestern Africa: Inferences from grain-size distributions of sediments on Walvis Ridge, SE Atlantic. *Marine Geology*, 180(1), 221–233. [https://doi.org/10.1016/S0025-3227\(01\)00215-8](https://doi.org/10.1016/S0025-3227(01)00215-8)
- Tamarin, T., & Kaspi, Y. (2016). The poleward motion of extratropical cyclones from a potential vorticity tendency analysis. *Journal of the Atmospheric Sciences*, 73(4), 1687–1707. <https://doi.org/10.1175/JAS-D-15-0168.1>
- Taylor, K. E., Stouffer, R. J., & Meehl, G. A. (2012). An overview of CMIP5 and the experiment design. *Bulletin of the American Meteorological Society*, 93(4), 485–498. <https://doi.org/10.1175/BAMS-D-11-00094.1>

- Thompson, A. F., & Naveira Garabato, A. C. (2014). Equilibration of the Antarctic circumpolar current by standing meanders. *Journal of Physical Oceanography*, 44(7), 1811–1828. <https://doi.org/10.1175/JPO-D-13-0163.1>
- Toggweiler, J. R. (1999). Variation of atmospheric CO₂ by ventilation of the ocean's deepest water. *Paleoceanography*, 14(5), 571–588. <https://doi.org/10.1029/1999PA900033>
- Toggweiler, J. R., Russell, J. L., & Carson, S. R. (2006). Midlatitude westerlies, atmospheric CO₂, and climate change during the ice ages. *Paleoceanography*, 21(2). <https://doi.org/10.1029/2005PA001154>
- Toggweiler, J. R., & Samuels, B. (1995). Effect of Drake Passage on the global thermohaline circulation. *Deep Sea Research Part I: Oceanographic Research Papers*, 42(4), 477–500. [https://doi.org/10.1016/0967-0637\(95\)00012-U](https://doi.org/10.1016/0967-0637(95)00012-U)
- Wang, Y. V., Leduc, G., Regenberg, M., Andersen, N., Larsen, T., Blanz, T., & Schneider, R. R. (2013). Northern and southern hemisphere controls on seasonal sea surface temperatures in the Indian Ocean during the last deglaciation. *Paleoceanography*, 28(4), 619–632. <https://doi.org/10.1002/palo.20053>
- Winn, K. (2013). Carbon and oxygen isotope ratios on planktonic foraminifera in subtropical Southeast Pacific core GIK17747-2 (p. 333 data points) [Text/tab-separated-values]. PANGAEA—Data Publisher for Earth & Environmental Science. <https://doi.org/10.1594/PANGAEA.815877>
- Wood, S. N. (2011). Fast stable restricted maximum likelihood and marginal likelihood estimation of semiparametric generalized linear models. *Journal of the Royal Statistical Society: Series B*, 73(1), 3–36. <https://doi.org/10.1111/j.1467-9868.2010.00749.x>
- Wood, S. N., Pya, N., & Säfken, B. (2016). Smoothing parameter and model selection for general smooth models. *Journal of the American Statistical Association*, 111(516), 1548–1563. <https://doi.org/10.1080/01621459.2016.1180986>
- Yang, H., Lohmann, G., Lu, J., Gowan, E. J., Shi, X., Liu, J., & Wang, Q. (2020). Tropical expansion driven by poleward advancing midlatitude meridional temperature gradients. *Journal of Geophysical Research: Atmospheres*, 125(16), e2020JD033158. <https://doi.org/10.1029/2020JD033158>
- Yin, J. H. (2005). A consistent poleward shift of the storm tracks in simulations of 21st century climate. *Geophysical Research Letters*, 32(18), L18701. <https://doi.org/10.1029/2005GL023684>
- Zahn, R., Pedersen, T. F., Kaminski, M. A., & Labeyrie, L. (Eds.) (1994). *Carbon cycling in the glacial ocean: Constraints on the Ocean's role in global change: Quantitative approaches in paleoceanography*. Springer-Verlag. <https://doi.org/10.1007/978-3-642-78737-9>
- Zika, J. D., Le Sommer, J., Dufour, C. O., Molines, J.-M., Barnier, B., Brasseur, P., et al. (2013). Vertical eddy fluxes in the Southern Ocean. *Journal of Physical Oceanography*, 43(5), 941–955. <https://doi.org/10.1175/JPO-D-12-0178.1>

References From the Supporting Information

- Akhoudas, C. H., Sallée, J.-B., Reverdin, G., Haumann, F. A., Pauthenet, E., Chapman, C. C., et al. (2023). Isotopic evidence for an intensified hydrological cycle in the Indian sector of the Southern Ocean. *Nature Communications*, 14(1), 2763. <https://doi.org/10.1038/s41467-023-38425-5>
- Boyer, T. P., Antonov, J. I., Baranova, O. K., Garcia, H. E., Johnson, D. R., Mishonov, A. V., et al. (2013). World ocean database 2013. <https://doi.org/10.7289/V5NZ85MT>
- Kalnay, E., Kanamitsu, M., Kistler, R., Collins, W., Deaven, D., Gandin, L., et al. (1996). The NCEP/NCAR 40-year reanalysis project. *Bulletin of the American Meteorological Society*, 77(3), 437–472. [https://doi.org/10.1175/1520-0477\(1996\)077<0437:tnyrp>2.0.co;2](https://doi.org/10.1175/1520-0477(1996)077<0437:tnyrp>2.0.co;2)
- LeGrande, A. N., & Schmidt, G. A. (2006). Global gridded data set of the oxygen isotopic composition in seawater. *Geophysical Research Letters*, 33(12), L12604. <https://doi.org/10.1029/2006GL026011>
- Lombard, F., Labeyrie, L., Michel, E., Bopp, L., Cortijo, E., Retaillieu, S., et al. (2011). Modelling planktic foraminifer growth and distribution using an ecophysiological multi-species approach. *Biogeosciences*, 8(4), 853–873. <https://doi.org/10.5194/bg-8-853-2011>
- Paren, J. G., & Potter, J. R. (1984). Isotopic tracers in polar seas and glacier ice. *Journal of Geophysical Research*, 89(C1), 749. <https://doi.org/10.1029/JC089iC01p00749>
- Strain, P. M., & Tan, F. C. (1993). Seasonal evolution of oxygen isotope-salinity relationships in high-latitude surface waters. *Journal of Geophysical Research*, 98(C8), 14589. <https://doi.org/10.1029/93JC01182>